

# Proposal for PAC37

## Deeply Virtual Compton Scattering on the Neutron with CLAS at 11 GeV

A. Fradi, B. Guegan, M. Guidal, S. Niccolai<sup>\*,†</sup>,  
S. Pisano, D. Sokhan (IPN Orsay)  
V. Koubarovski <sup>\*(Jefferson Lab)</sup>  
A. El Alaoui<sup>\*(Argonne National Laboratory)</sup>  
M. Aghasyan, S. Anefalos Pereira, E. De Sanctis,  
D. Hasch, V. Lucherini, M. Mirazita,<sup>\*</sup> P. Rossi (INFN Frascati)  
M. Battaglieri, R. De Vita, M. Osipenko, G. Ricco,  
M. Ripani, M. Taiuti (INFN Genova)  
C. Maieron, Y. Perrin, E. Voutier (LPSC Grenoble)  
J. Ball, M. Garçon, P. Konczykowski,  
B. Moreno, H. Moutarde, S. Procureur, F. Sabatié (SPhN-CEA Saclay)  
A. D'Angelo, C. Schaerf, V. Vegna (Università di Roma 2 - Tor Vergata)  
J. Annand, M. Hoek, D. Ireland, R. Kaiser,  
K. Livingston, G. Rosner, B. Seitz, G. Smith (University of Glasgow)  
L. Barion, M. Contalbrigo, G. Ciullo, P. Lenisa, L. Pappalardo (INFN Ferrara)  
F. Meddi, G.M. Urcioli (INFN Roma)  
D.M. Castelluccio, E. Cisbani, F. Garibaldi, S. Frullani (INFN Roma - Sanità)  
M. Capogni (INFN Roma and ENEA Casaccia)  
V. Bellini, A. Giusa, F. Mammoliti, G. Russo,  
L. Sperduto, C. Sutura (INFN Catania and Università di Catania)  
R. De Leo (Università di Bari)  
R. Perrino (INFN Lecce)

November 20, 2010

---

<sup>\*</sup>co-spokesperson

<sup>†</sup>contact person, email: [silvia@jlab.org](mailto:silvia@jlab.org)

## Abstract

Measuring Deeply Virtual Compton Scattering on a neutron target is one of the necessary steps to complete our understanding of the structure of the nucleon in terms of Generalized Parton Distributions. DVCS on a neutron target plays a complementary role to the one on a transversely polarized proton target in the determination of the GPD  $E$ , the least known and least constrained GPD that enters Ji's angular momentum sum rule. We propose to measure beam-spin asymmetries for neutron DVCS ( $ed \rightarrow e'n\gamma(p)$ ) with the upgraded 11-GeV CEBAF polarized-electron beam and the CLAS12 detector. For the detection of the recoil neutron, necessary to ensure the exclusivity of the reaction after having detected the scattered electron and the DVCS photon, we will construct a scintillator-barrel detector to be placed in the Central Detector, between the CTOF and the solenoid magnet. This Central Neutron Detector (CND) will be made of three layers of scintillator paddles (48 paddles per layer), coupled two-by-two at the front with semi-circular light guides and read at the back by photomultipliers placed outside of the high magnetic-field region and connected to the bars via 1-meter-long bent light guides. Simulations and R&D studies have proven the experimental feasibility of this project. A prototype of the CND, covering two of the 48 azimuthal bins, is under construction. In order to achieve average relative statistical errors of about 15% on 2160 4-dimensional ( $Q^2$ ,  $x_B$ ,  $-t$ ,  $\phi$ ) kinematic bins, we request 80 days of running on a deuteron target.

# Contents

<b>1</b>	<b>Introduction</b>	<b>7</b>
<b>2</b>	<b>Physics motivation: neutron GPDs</b>	<b>8</b>
<b>3</b>	<b>Kinematics for nDVCS at 11 GeV</b>	<b>11</b>
<b>4</b>	<b>Central Neutron Detector: motivation and requirements</b>	<b>11</b>
<b>5</b>	<b>CND: R &amp; D studies and final detector design</b>	<b>21</b>
5.1	Summary of early R&D studies . . . . .	24
5.2	Final design and performances . . . . .	25
<b>6</b>	<b>Simulation and reconstruction</b>	<b>30</b>
6.1	Efficiency . . . . .	30
6.2	Particle Identification . . . . .	30
6.3	Angular and momentum resolutions . . . . .	33
<b>7</b>	<b>Count-rate estimate</b>	<b>37</b>
<b>8</b>	<b><math>en\pi^0(p)</math> background</b>	<b>37</b>
<b>9</b>	<b>Backgrounds on the CND</b>	<b>41</b>
9.1	Physics background . . . . .	41
9.2	Electromagnetic background - THE MC JOBS FOR THIS SECTION ARE STILL RUNNING, NUMBERS TO BE UPDATED IN THE NEXT DAYS .	42
<b>10</b>	<b>Summary and conclusions</b>	<b>44</b>
<b>11</b>	<b>Appendix: details on simulation and reconstruction</b>	<b>47</b>
11.1	Digitisation of signals from CND paddles (in GEMC) . . . . .	47
11.2	Hit reconstruction . . . . .	48

## List of Tables

- |   |   |    |
|---|---|----|
| 1 | Expected 4-fold differential cross sections, 4-dimensional acceptance and number of events for nDVCS with CLAS12 and the CND, as a function of $\phi$ . $\langle t \rangle = -0.4 \text{ GeV}^2$ , $\langle Q^2 \rangle = 2.5 \text{ GeV}^2$ , $\langle x_B \rangle = 0.14$ , $\Delta\phi = 30^\circ$ , $\Delta Q^2 = 1 \text{ GeV}^2$ , $\Delta x_B = 0.08$ , $\Delta t = 0.2 \text{ GeV}^2$ . The calculation was done for a luminosity $L = 10^{35} \text{ cm}^{-2}\text{s}^{-1}$ and for 80 days of running time. . . . . | 40 |
|---|---|----|

## List of Figures

- |   |  |    |
|---|--|----|
| 1 | The handbag diagram for the DVCS process on a nucleon $eN \rightarrow e'N'\gamma'$ . Here $x + \xi$ and $x - \xi$ are the longitudinal momentum fractions of the initial and final quark, respectively, and $t = (p - p')^2$ is the squared momentum transfer between the initial and final protons (or equivalently between the two photons). There is also a crossed diagram which is not shown here. . . . .  | 7  |
| 2 | Predicted beam-spin asymmetry for DVCS on a neutron target, plotted as a function of (from left to right) $\phi$ , $-t$ , $x_B$ , and $Q^2$ . The kinematics are: $E_e=11 \text{ GeV}$ , $x_B=0.17$ , $Q^2=2 \text{ GeV}^2$ , $-t=0.4 \text{ GeV}^2$ and $\phi=60^\circ$ . All distributions have been calculated at these kinematics, except for the variable against which each distribution is plotted. The curves are obtained for different combinations of values of $J_u$ and $J_d$ : ( $J_u = 0.3, J_d = 0.1$ ) - solid curve, ( $J_u = 0.8, J_d = 0.1$ ) - thin dashed curve, ( $J_u = -0.5, J_d = 0.1$ ) - thin dash-dotted curve, ( $J_u = 0.3, J_d = 0.8$ ) - thick dashed curve, ( $J_u = 0.3, J_d = -0.5$ ) - thick dash-dotted curve. . . . . | 10 |
| 3 | Beam-spin asymmetry for DVCS on a proton target, plotted as a function of (from left to right) $\phi$ , $-t$ , $x_B$ and $Q^2$ , as predicted by the VGG model. $E_e=11 \text{ GeV}$ , $x_B=0.2$ , $Q^2=2 \text{ GeV}^2$ , $-t=0.2 \text{ GeV}^2$ and $\phi=60^\circ$ . Otherwise, same conditions and conventions as for Fig. 2. . . . .  | 12 |
| 4 | Unpolarized cross section for DVCS on a proton target (solid curves) and on a neutron target (dashed curve), plotted as a function of (from left to right) $\phi$ , $-t$ and $x_B$ . Same kinematics as for Fig. 3 (for the proton) and Fig. 2 (for the neutron). . . . .  | 13 |
| 5 | $Q^2$ as a function of $x_B$ , for nDVCS events. Forward-CLAS12 acceptance cuts and physics cuts are included. . . . .   | 14 |
| 6 | $t$ as a function of $x_B$ , for nDVCS events. Forward-CLAS12 acceptance cuts and physics cuts are included. . . . .   | 14 |
| 7 | $t$ as a function of $Q^2$ , for nDVCS events. Forward-CLAS12 acceptance cuts and physics cuts are included. . . . .   | 15 |
| 8 | Electron energy as a function of electron polar angle, for nDVCS events. Forward-CLAS12 acceptance cuts and physics cuts are included. . . . .   | 15 |
| 9 | Photon energy as a function of photon polar angle, for nDVCS events. Forward-CLAS12 acceptance cuts and physics cuts are included. The two zones correspond to the IC/Forward tagger (from 2 to 5 degrees) and to the FEC (from 5 degrees onwards). . . . .  | 16 |

10	Neutron momentum as a function of neutron polar angle, for nDVCS events. Forward-CLAS12 acceptance cuts and physics cuts are included. . . . .	16
11	Neutron momentum distribution, for nDVCS events. Forward-CLAS12 acceptance cuts and physics cuts are included. . . . .	17
12	Neutron polar angle, for nDVCS events. Forward-CLAS12 acceptance cuts and physics cuts are included. . . . .	17
13	Missing mass squared of the $e'n\gamma$ system, for the nDVCS channel, simulated with our event generator, assuming absolute precision on the photon and electron kinematic variables, fixing the neutron angular resolutions and varying the momentum resolution between 0.1% and 20%. . . . .	19
14	Missing mass squared of the $e'n\gamma$ system, for the nDVCS channel, simulated with our event generator, assuming absolute precision on the photon and electron kinematic variables, fixing the neutron momentum and $\phi$ resolutions and varying the $\theta$ resolution between $0.1^\circ$ and $20^\circ$ . . . . .	20
15	Missing mass squared of the $e'n\gamma$ system, for the nDVCS channel, simulated with our event generator, assuming absolute precision on the photon and electron kinematic variables, fixing the neutron momentum and $\theta$ resolutions and varying the $\phi$ resolution between $0.1^\circ$ and $20^\circ$ . . . . .	21
16	Missing mass squared of the $e'n\gamma$ system, for the nDVCS channel, simulated with our event generator, assuming the nominal CLAS12 resolutions on the photon and electron kinematic variables, fixing the neutron $\theta$ and $\phi$ resolutions and varying the momentum resolution, between 0.1% and 20%. . . . .	22
17	Missing mass squared of the $e'n\gamma$ system, for the nDVCS channel, simulated with our event generator. The different colors correspond to different combinations of choices of particles being detected with absolute precision or with realistic resolutions. . . . .	23
18	Drawing of the Central Detector: the red area represents the free space between the magnet and the CTOF. . . . .	23
19	Geometry of the Central Neutron Detector. The current design consists of 3 radial layers each made by 48 trapezoidal scintillator paddles. . . . .	24
20	Magnetic field map for the Central Detector (radial component on the top, axial component on the bottom. The black line in the top plot shows the position of the PMTs of the Central Neutron Detector. . . . .	26
21	Drawing (side view) of the CND, placed into the solenoid magnet. . . . .	26
22	The one-layer prototype of the CND during the timing resolution measurements with cosmic rays carried out at Orsay. . . . .	27
23	Drawing of the three-layer prototype of the CND, under construction. . . . .	27
24	Charge collected by the two PMTs as a function of the position of the trigger for the one-layer prototype. . . . .	28
25	Time resolution of each PMT as a function of the position of the trigger for the one-layer prototype. . . . .	29
26	Efficiency for the detection of neutrons having 0.4 GeV/c of momentum, as a function of the threshold on the deposited energy. The efficiency is shown for 3 different values of $\theta_n$ , between $50^\circ$ and $90^\circ$ . . . . .	31

27	Efficiency for the detection of neutrons emitted at $60^\circ$ , as a function of momentum, for 7 different values of the threshold on the deposited energy, from 1 to 5 MeV. . . . .	31
28	Efficiency for the detection of neutrons, as a function of neutron momentum, for a 2-MeV threshold on the deposited energy. The efficiency is shown for three different values of $\theta_n$ , between $50^\circ$ and $70^\circ$ . . . . .	32
29	Efficiency for the detection of photons, as a function of photon momentum, for a 2-MeV threshold on the deposited energy. The efficiency is shown for $\theta_\gamma = 60^\circ$ . . . . .	32
30	$\beta$ distributions for neutrons with $p_n = 0.2$ GeV/c (green), $p_n = 0.4$ GeV/c (purple), $p_n = 0.7$ GeV/c (blue), $p_n = 1$ GeV/c (red), and photons with $E = 1$ GeV. Each box shows the results for one of the three radial layers that compose the CND (the innermost is on the top, the outermost is on the bottom). The threshold on the deposited energy is 2 MeV. The plots show all hits, integrated over $\phi$ . Equal neutron and photon yields have been assumed here. . . . .	34
31	$\beta$ versus momentum for neutrons (red) and photons (blue) with momenta between 0.2 and 1 GeV. The error bars are defined as $3\sigma$ , where $\sigma$ is the fitted width of each $\beta$ peak. The threshold on the deposited energy is 2 MeV. . . . .	35
32	Angular resolution $\sigma_\theta$ as a function of $\theta$ for neutrons of momentum 0.4 GeV/c, for a 2-MeV threshold on the deposited energy. The three colors of the points correspond to the three radial layers of the CND. . . . .	36
33	Momentum resolution $\sigma_p/p$ as a function of $p$ for neutrons having $\theta = 60^\circ$ , for a 2-MeV threshold on the deposited energy. The three colors of the points correspond to the three radial layers of the CND. . . . .	36
34	Beam-spin asymmetry for nDVCS as predicted by the VGG model (for $J_u = .3$ and $J_d = .1$ ), plotted as a function of $\phi$ for the kinematic bin $t = -0.4$ GeV <sup>2</sup> , $Q^2 = 2.5$ GeV <sup>2</sup> , $x_B = 0.14$ . The error bars reflect the expected uncertainties for our experiment, corresponding to 80 hours of beam time at a luminosity of $10^{35}$ . . . . .	38
35	Top: cross section for nDVCS. Middle: acceptance for the nDVCS channel, including only CLAS12, computed with our event generator + FASTMC. Bottom: expected count rate for 80 days of beam time. All three plots are produced for the kinematic bin of Table 7. . . . .	39
36	Missing mass of the $e'n\gamma$ system, for the nDVCS channel (in red), and the $ed \rightarrow e'n\pi^0(p)$ channel (in black), both simulated with our event generator. "Realistic" CLAS12 and CND resolutions are applied. . . . .	41
37	View (from the beam's perspective) of the Central Detector, for one simulated "background event". Red tracks correspond to negatively charged particles, green tracks correspond to neutrals. This picture has been obtained for a luminosity $L = 10^{33}$ cm <sup>-2</sup> s <sup>-1</sup> , corresponding to 1/100 of the nominal luminosity, for practical reasons related to the graphical interface. . . . .	43

38	Distribution of the energy deposit in the CND, integrated over all the azimuthal and radial bins, of the hits coming from the generated electromagnetic background. The majority of the events correspond to an energy release below 1 MeV. . . . .	44
39	Event distribution for the electromagnetic background in the CND, as a function of the $x$ and $y$ coordinates in the lab frame ( $z$ being the beam direction), without any cut on the deposited energy. It can be seen that the majority of the events are concentrated in the innermost layers of the CND. . . . .	45

# 1 Introduction

Generalized Parton Distributions are nowadays the object of an intense effort of research, in the perspective of understanding nucleon structure. They describe the correlations between the longitudinal momentum and transverse spatial position of the partons inside the nucleon, they give access to the contribution of the orbital momentum of the quarks to the nucleon spin, they are sensitive to the correlated  $q - \bar{q}$  components, etc. The original articles and general reviews on GPDs and details on the formalism can be found in Refs. [1, 2, 3, 4, 5, 6, 7].

The nucleon GPDs are the structure functions which are accessed in the measurement of the exclusive leptonproduction of a photon (DVCS, which stands for Deeply Virtual Compton Scattering) or of a meson on the nucleon, at sufficiently large  $Q^2$ , where  $Q^2$  is the virtuality of the photon emitted by the initial lepton. Figure 1 illustrates such kind of process. Considering only helicity-conserving quantities and the quark sector, there are four GPDs,  $H, \tilde{H}, E, \tilde{E}$ , which depend, in leading-order and leading-twist QCD, upon three variables:  $x, \xi$  and  $t$ .  $x - \xi$  and  $x + \xi$  are the longitudinal momentum fractions of the quarks, respectively, coming out and going back into the nucleon and  $t$  is the squared four-momentum transfer between the final and initial nucleon.

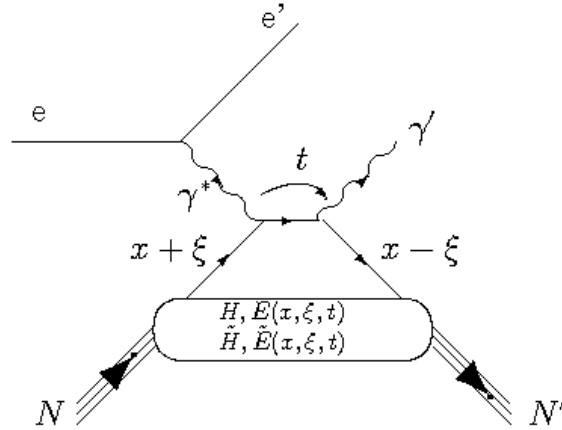


Figure 1: The handbag diagram for the DVCS process on a nucleon  $eN \rightarrow e'N'\gamma'$ . Here  $x + \xi$  and  $x - \xi$  are the longitudinal momentum fractions of the initial and final quark, respectively, and  $t = (p - p')^2$  is the squared momentum transfer between the initial and final protons (or equivalently between the two photons). There is also a crossed diagram which is not shown here.

Among the three variables,  $x, \xi$  and  $t$ , only two,  $\xi$  and  $t$ , are accessible experimentally (in the Bjorken limit,  $\xi = \frac{x_B/2}{1-x_B/2}$ , where  $x_B$  is the standard Bjorken variable). Formally, the



DVCS amplitude is proportional to:

$$\int_{-1}^{+1} dx \frac{H(\mp x, \xi, t)}{x \pm \xi \mp i\epsilon} + \dots \quad (1)$$

(where the ellipsis stands for similar terms for  $E$ ,  $\tilde{H}$  and  $\tilde{E}$ ).

Decomposing this expression into its real and imaginary part, it is found that the maximum information that can be extracted from the experimental data at a given  $(\xi, t)$  point is  $H(\pm\xi, \xi, t)$ , when measuring an observable sensitive to the imaginary part of the DVCS amplitude, and  $\int_{-1}^{+1} dx \frac{H(\mp x, \xi, t)}{x \pm \xi}$ , when measuring an observable sensitive to the real part of the DVCS amplitude. Knowing the GPDs at some particular point  $(\pm\xi, \xi, t)$  and their weighted integral over  $x$  does not, of course, uniquely define them. Therefore, unavoidably, a model input will be required, to make the interpolation over the variable  $x$ .

The DVCS process is accompanied by the Bethe-Heitler (BH) process, in which the final-state photon is radiated by the incoming or scattered electron and not by the nucleon itself. The BH process, which is not sensitive to GPDs, is experimentally indistinguishable from the DVCS and interferes with it, complicating the matter. However, considering that the nucleon form factors are well known at small  $t$ , the BH process is precisely calculable theoretically.

It is therefore clearly a highly non-trivial task to actually measure the GPDs. It calls for a long-term experimental program comprising the measurement of different observables: cross sections, beam-, longitudinal and transverse target- single polarization observables, double polarization observables and also possibly beam-charge asymmetries, timelike Compton scattering, etcetera. Ref. [8] shows the information brought by the various observables.

Such dedicated experimental program, concentrating on a proton target, has started worldwide in these past few years. JLab has provided the first measurement, in the valence region, of beam-polarized and unpolarized DVCS cross sections, in a limited phase-space domain, in the Hall A [9], and several beam-spin asymmetries (BSA), over a large kinematic range, obtained with the CLAS detector [10]. Beam-charge asymmetries, BSAs and transversely-polarized target-spin asymmetries have also been measured by the HERMES collaboration [11]. These first data will soon be completed with a series of new experiments ongoing and planned at JLab and aimed to measure accurately longitudinally [12] and transversely [13] polarized target-spin asymmetries and cross sections (along with double-polarization observables) and new precise unpolarized and beam-polarized cross sections at new kinematics [14, 15]. Measurements of DVCS cross sections and BSA with JLab at 12 GeV have also been recently proposed [16, 17].

## 2 Physics motivation: neutron GPDs

The aim of this proposal is to start a similar experimental program with a neutron target. The importance of neutron targets in the DVCS phenomenology was clearly established in the pioneering Hall A experiment, where the beam-polarized cross section off a neutron, from a deuterium target, was measured [18].

Measuring neutron GPDs is highly complementary to measuring proton GPDs. Neutron and proton GPDs are independent quantities, like neutron and proton form factors. However, measuring both GPDs allows to carry out a flavor separation. For instance,

$$H^p(\xi, \xi, t) = \frac{4}{9}H^u(\xi, \xi, t) + \frac{1}{9}H^d(\xi, \xi, t), \quad (2)$$

while

$$H^n(\xi, \xi, t) = \frac{1}{9}H^u(\xi, \xi, t) + \frac{4}{9}H^d(\xi, \xi, t) \quad (3)$$

(and similarly for  $E$ ,  $\tilde{H}$  and  $\tilde{E}$ ).

Also, concerning the BSA, which is the main goal of this proposal, it can be shown that, in the case of DVCS on the neutron, its amplitude is mainly governed by the GPD  $E$ , the least known of the GPDs. In particular,  $E$  is one of the two GPDs entering Ji's sum rule:

$$J_q = \frac{1}{2} \int_{-1}^{+1} dx x [H^q(x, \xi, t=0) + E^q(x, \xi, t=0)], \quad (4)$$

which links the total angular momentum carried by each quark  $q$  ( $J_q$ ) to the sum of the second moments over  $x$  of the GPDs  $H$  and  $E$ . It is therefore crucial to obtain experimental constraints on  $E$  in order to make some first steps towards the estimation of the contribution of the orbital momentum of the quarks to the nucleon spin. In order to make a quark-flavor separation, both  $E^n$  and  $E^p$  are needed: this proposal mainly aims at  $E^n$ .  $E^p$  can be accessed through transverse-target polarization or double (beam-target) polarization observables on the proton [8], which are, as previously mentioned, the goals of experiments already planned at JLab.

Hereafter, the VGG model [19, 20], which parametrizes GPDs and calculates the associated DVCS observables, has been adopted, in order to quantify (albeit in a model-dependent way) the sensitivity of the neutron-DVCS BSA to the GPD  $E$ . An interesting feature of the VGG model is that the parametrization of the GPD  $E$  is dependent on the two parameters  $J_u$  and  $J_d$ , i.e. the total spin (orbital momentum+intrinsic spin) contributions of the  $u$  and  $d$  quarks respectively. The idea is that a given shape in  $x$  for the GPD  $E^q$  is assumed, and then the overall normalization is proportional to  $J_q$  (see ref. [5] for more details). Figure 2 shows the BSA for nDVCS as a function of the four independent variables describing the DVCS process,  $\phi$ ,  $-t$ ,  $x_B$  and  $Q^2$ , for different values of  $J_u$  and  $J_d$ , as predicted by the VGG model. The kinematics for Fig. 2 are  $E_e=11$  GeV,  $x_B=0.17$ ,  $Q^2=2$  GeV<sup>2</sup>,  $-t=0.4$  GeV<sup>2</sup> and  $\phi=60^\circ$ . Although some of the  $J_u$ ,  $J_d$  values are probably unrealistic (for instance  $J_d=0.8$ , which would imply that 80% of the spin of the proton comes from the  $d$  quark), nevertheless, this shows the strong sensitivity of this BSA to  $E$  and, in the framework of the VGG model, to  $J_q$ . One sees that these BSAs can extend from 10 to 50%, with spectacular changes of sign depending on the relative signs of  $J_u$  and  $J_d$ , and therefore they can be as large, in magnitude, as the proton-DVCS beam-spin asymmetries that have been recently measured [10]. However, it is important to notice that these “large” neutron-DVCS asymmetries are obtained only in a specific phase space region, i.e. only around  $x_B=0.1$  or  $0.15$ . To reach such “low” values of  $x_B$ , at sufficiently large  $Q^2$ , an 11-GeV electron beam is needed. The current 6-GeV beam allows to explore mainly the  $x_B \approx 0.35$  region where the BSA is not maximum at all. This is confirmed by the exploratory measurement of the JLab Hall A collaboration [18] where neutron-DVCS BSAs essentially consistent with zero were obtained and for which the sensitivity to  $J_q$  was therefore minimal.

Figure 3 shows the corresponding BSAs, at approximatively the same kinematics, for the proton case. It is clear that the sensitivity to  $E$  or, alternatively to  $J_u$  and  $J_d$ , is much less.

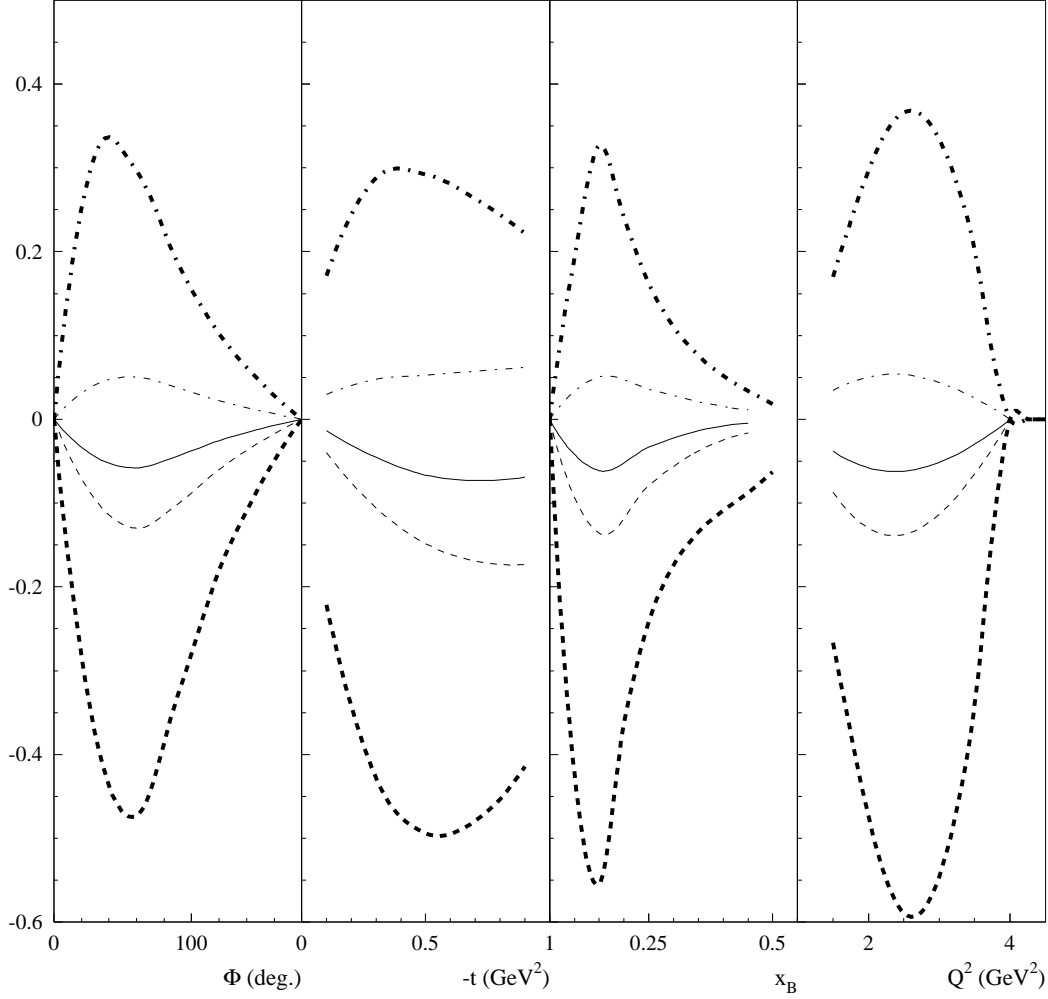


Figure 2: Predicted beam-spin asymmetry for DVCS on a neutron target, plotted as a function of (from left to right)  $\phi$ ,  $-t$ ,  $x_B$ , and  $Q^2$ . The kinematics are:  $E_e=11$  GeV,  $x_B=0.17$ ,  $Q^2=2$  GeV<sup>2</sup>,  $-t=0.4$  GeV<sup>2</sup> and  $\phi=60^\circ$ . All distributions have been calculated at these kinematics, except for the variable against which each distribution is plotted. The curves are obtained for different combinations of values of  $J_u$  and  $J_d$ : ( $J_u = 0.3, J_d = 0.1$ ) - solid curve, ( $J_u = 0.8, J_d = 0.1$ ) - thin dashed curve, ( $J_u = -0.5, J_d = 0.1$ ) - thin dash-dotted<sup>10</sup> curve, ( $J_u = 0.3, J_d = 0.8$ ) - thick dashed curve, ( $J_u = 0.3, J_d = -0.5$ ) - thick dash-dotted curve.

This is mainly due to the fact that the proton-DVCS BSA is mainly sensitive to the  $H$  GPD, the weight of the  $E$  GPD being suppressed by kinematical factors.

Finally, Fig. 4 shows the comparison of the unpolarized cross sections for DVCS on the proton and on the neutron at approximately the same kinematics, as a function of  $\phi$ ,  $-t$  and  $x_B$ , according to the VGG model with  $J_u = 0.3$  and  $J_d = 0.1$ . One sees that the neutron-DVCS cross sections are, depending on the kinematics, a factor 3 to 5 below the proton-DVCS cross sections.

### 3 Kinematics for nDVCS at 11 GeV

An event generator for DVCS and exclusive  $\pi^0$  electroproduction on the neutron inside a deuterium target has been developed [21]. The DVCS amplitude is calculated according to the BKM formalism [22], while the GPDs have been taken from the standard CLAS DVCS generator [23]. The Fermi-motion distribution is calculated with the Paris potential [24].

The output of the event generator was fed through CLAS12 FASTMC, to simulate the acceptance and resolutions of electrons and photons in the Forward Detector. The IC-Forward tagger, covering polar angles between  $2^\circ$  and  $5^\circ$  has also been included for the photon detection. Kinematic cuts to ensure the applicability of the GPD formalism ( $Q^2 > 1 \text{ GeV}^2/c^2$ ,  $t > -1.2 \text{ GeV}^2/c^2$ ,  $W > 2 \text{ GeV}/c^2$ ), have been applied. Figures 5, 6, and 7 show the coverage in  $Q^2$ ,  $x_B$  and  $t$  that is obtained from the event generator for the nDVCS reaction, with an electron-beam energy of 11 GeV.

Figures 8, 9, and 10 show  $\theta$  as a function of momentum in the lab frame for, respectively, the electron, the photon and the neutron. Figures 11 and 12 are one-dimensional plots, showing, respectively, the momentum and the polar angle of the recoil neutron. As expected, the electron and the photon are mostly emitted at forward angles, while the recoil neutron is going at backwards angles.

### 4 Central Neutron Detector: motivation and requirements

In the hypothesis of absence of Final State Interactions (FSI), the minimal requirement to ensure the exclusivity of the nDVCS reaction and to determine the final and initial state is to fully detect (PID, angles and momentum) the scattered electron, the photon, and the neutron. In fact, using four-vectors, the energy-momentum conservation for the nDVCS reaction can be written as:

$$p_e^\mu + p_n^\mu + p_p^\mu = p_{e'}^\mu + p_{n'}^\mu + p_{p'}^\mu + p_\gamma^\mu. \quad (5)$$

The absence of FSI implies that the kinematics of the initial and final spectator proton are equal:

$$p_p^\mu = p_{p'}^\mu. \quad (6)$$

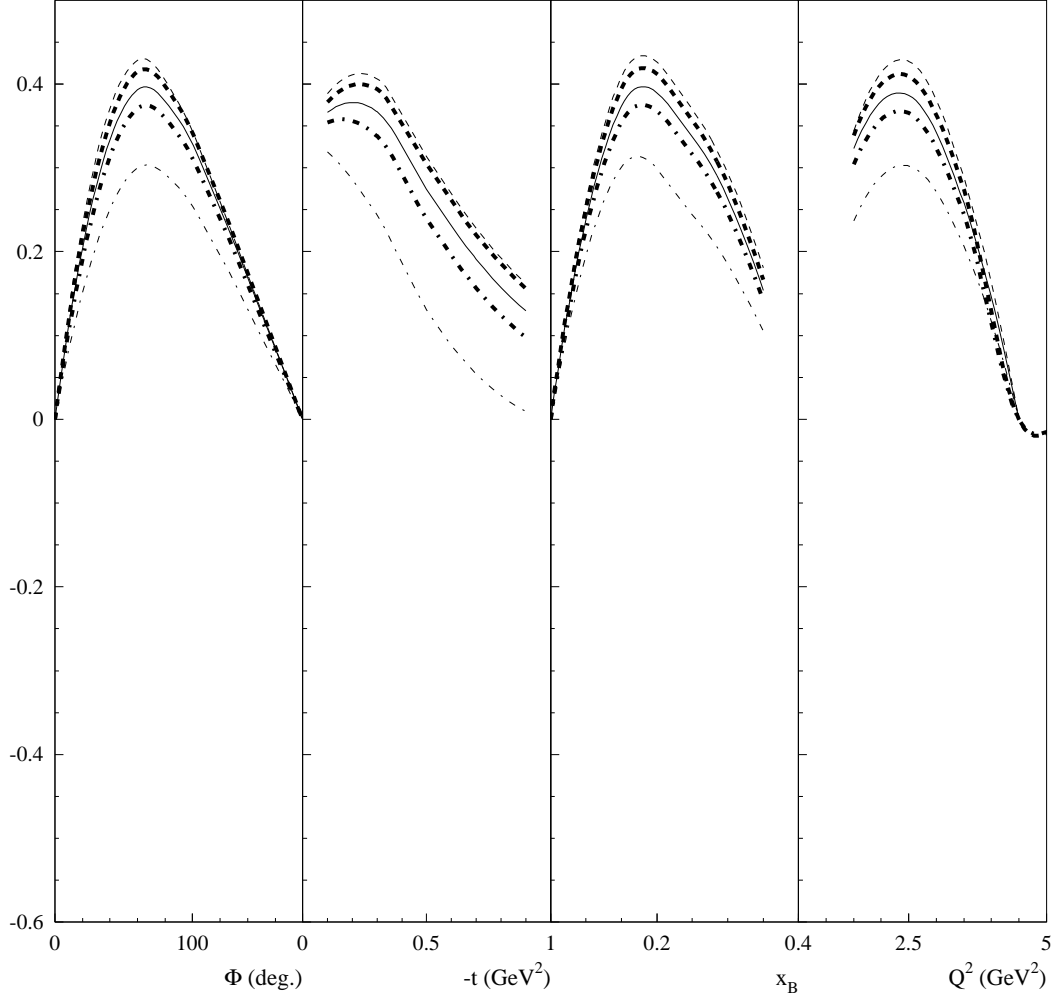


Figure 3: Beam-spin asymmetry for DVCS on a proton target, plotted as a function of (from left to right)  $\phi$ ,  $-t$ ,  $x_B$  and  $Q^2$ , as predicted by the VGG model.  $E_e=11$  GeV,  $x_B=0.2$ ,  $Q^2=2$  GeV<sup>2</sup>,  $-t=0.2$  GeV<sup>2</sup> and  $\phi=60^\circ$ . Otherwise, same conditions and conventions as for Fig. 2.

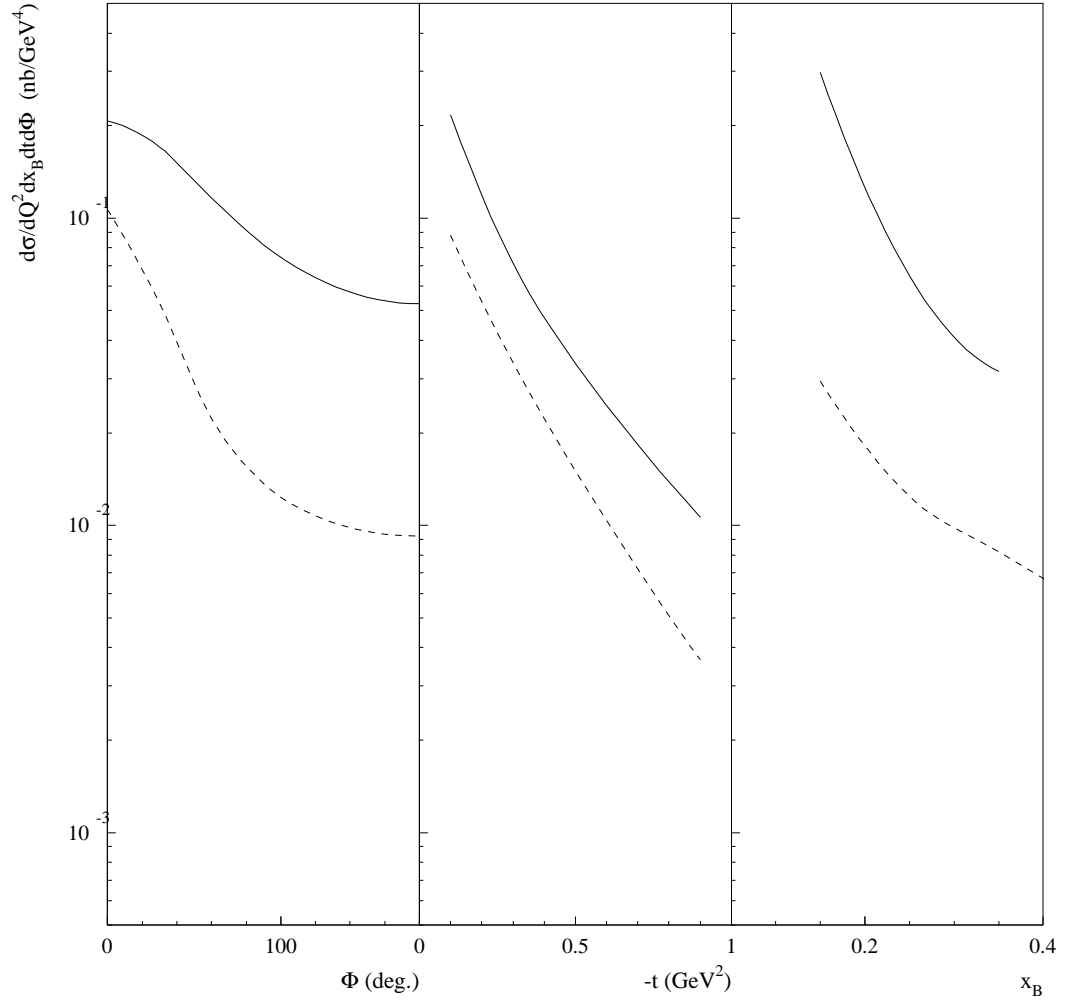


Figure 4: Unpolarized cross section for DVCS on a proton target (solid curves) and on a neutron target (dashed curve), plotted as a function of (from left to right)  $\phi$ ,  $-t$  and  $x_B$ . Same kinematics as for Fig. 3 (for the proton) and Fig. 2 (for the neutron).

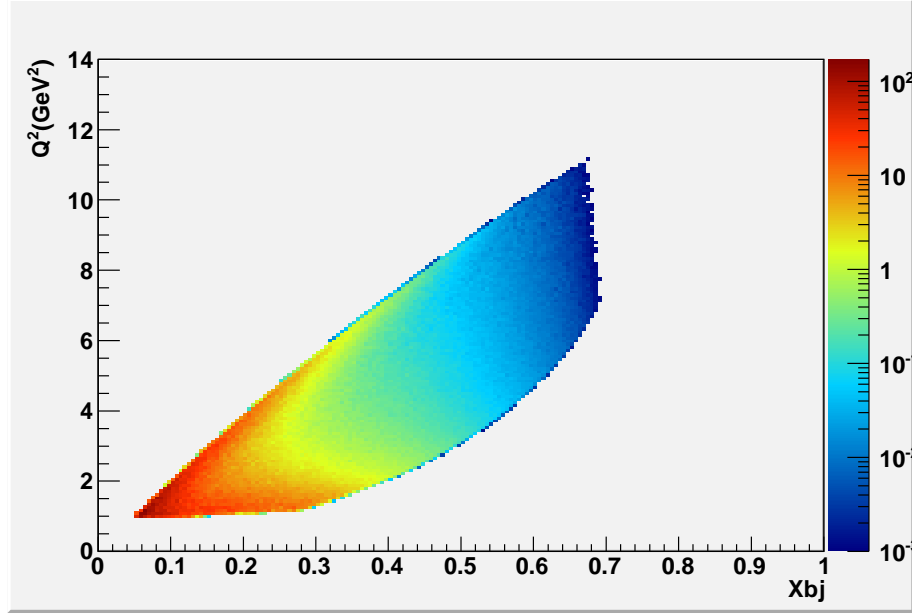


Figure 5:  $Q^2$  as a function of  $x_B$ , for nDVCS events. Forward-CLAS12 acceptance cuts and physics cuts are included.

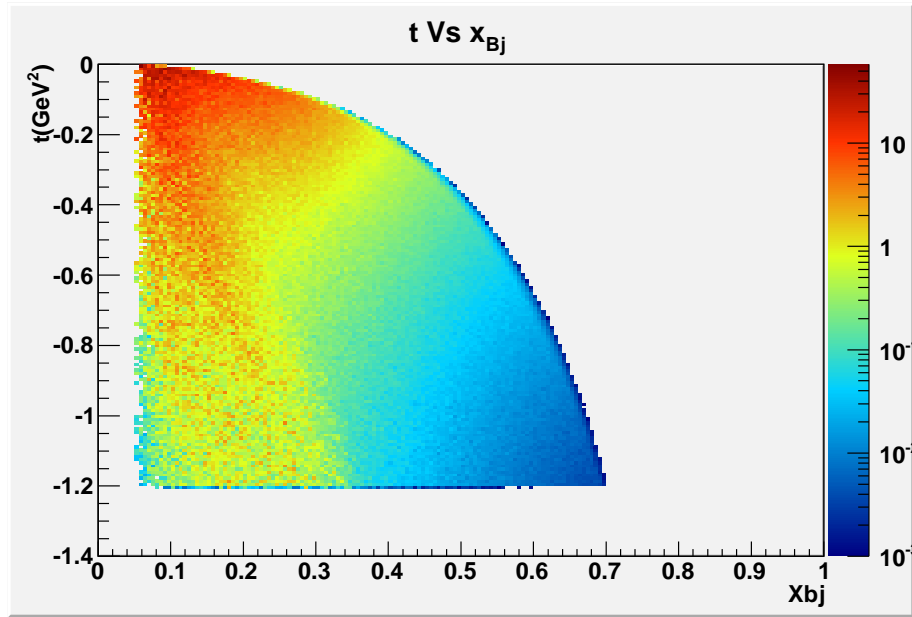


Figure 6:  $t$  as a function of  $x_B$ , for nDVCS events. Forward-CLAS12 acceptance cuts and physics cuts are included.

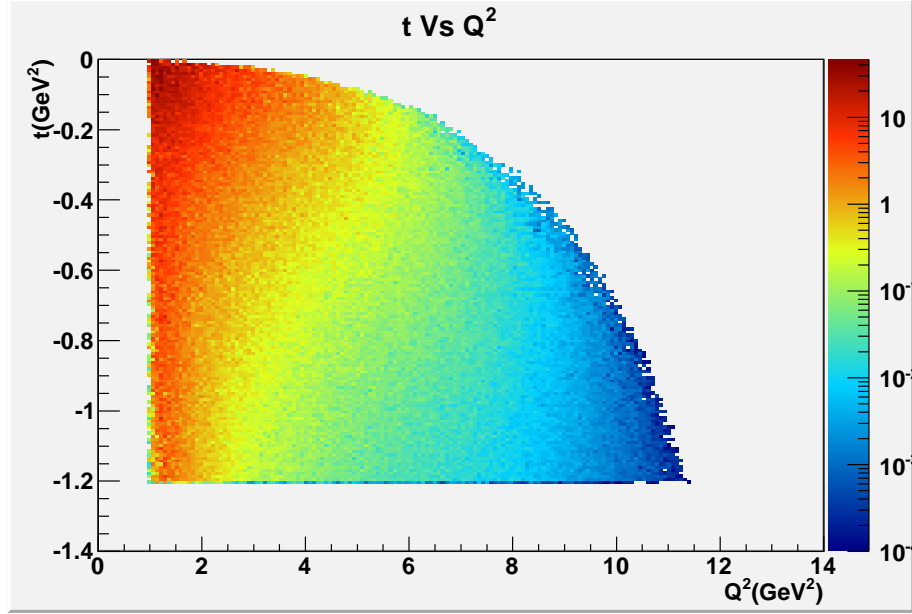


Figure 7:  $t$  as a function of  $Q^2$ , for nDVCS events. Forward-CLAS12 acceptance cuts and physics cuts are included.

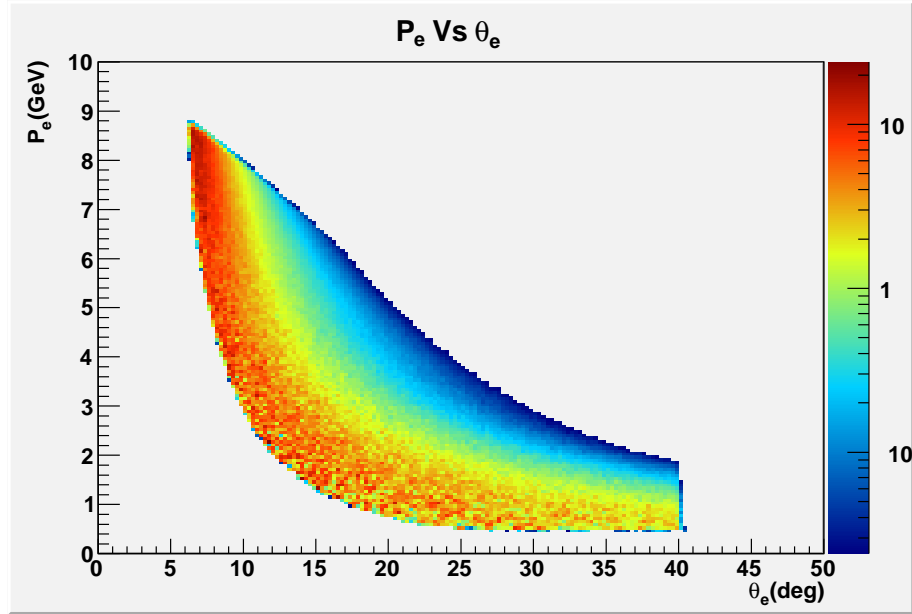


Figure 8: Electron energy as a function of electron polar angle, for nDVCS events. Forward-CLAS12 acceptance cuts and physics cuts are included.



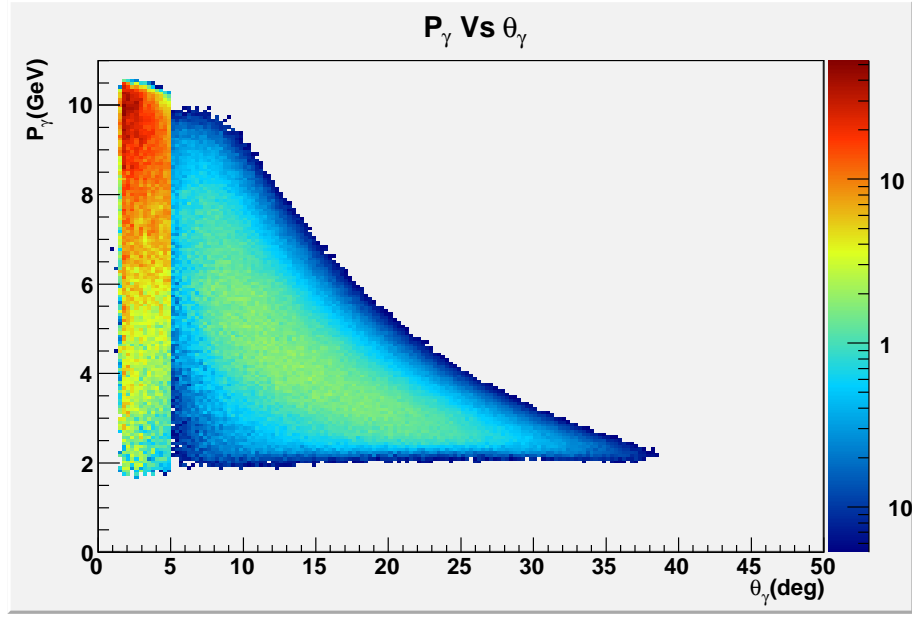


Figure 9: Photon energy as a function of photon polar angle, for nDVCS events. Forward-CLAS12 acceptance cuts and physics cuts are included. The two zones correspond to the IC/Forward tagger (from 2 to 5 degrees) and to the FEC (from 5 degrees onwards).

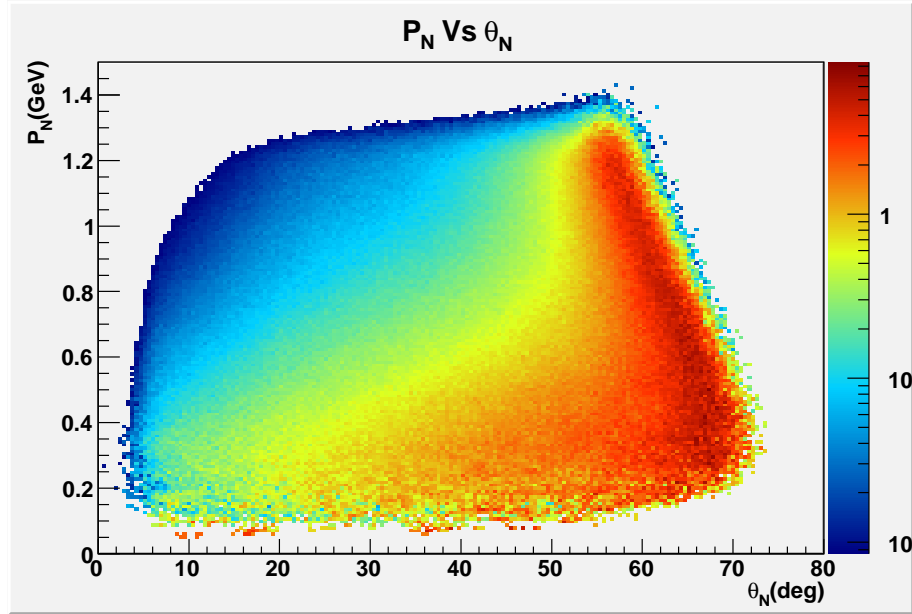


Figure 10: Neutron momentum as a function of neutron polar angle, for nDVCS events. Forward-CLAS12 acceptance cuts and physics cuts are included.

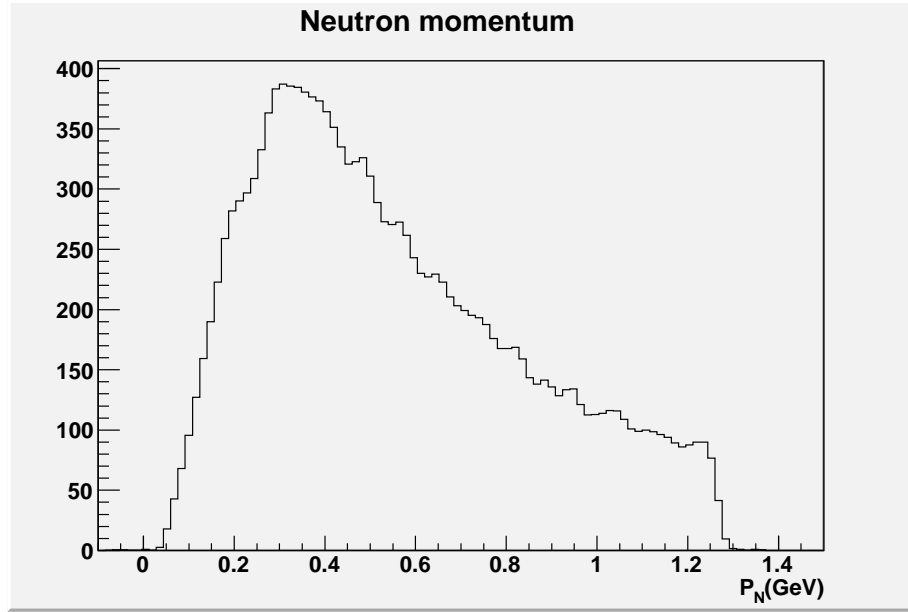


Figure 11: Neutron momentum distribution, for nDVCS events. Forward-CLAS12 acceptance cuts and physics cuts are included.

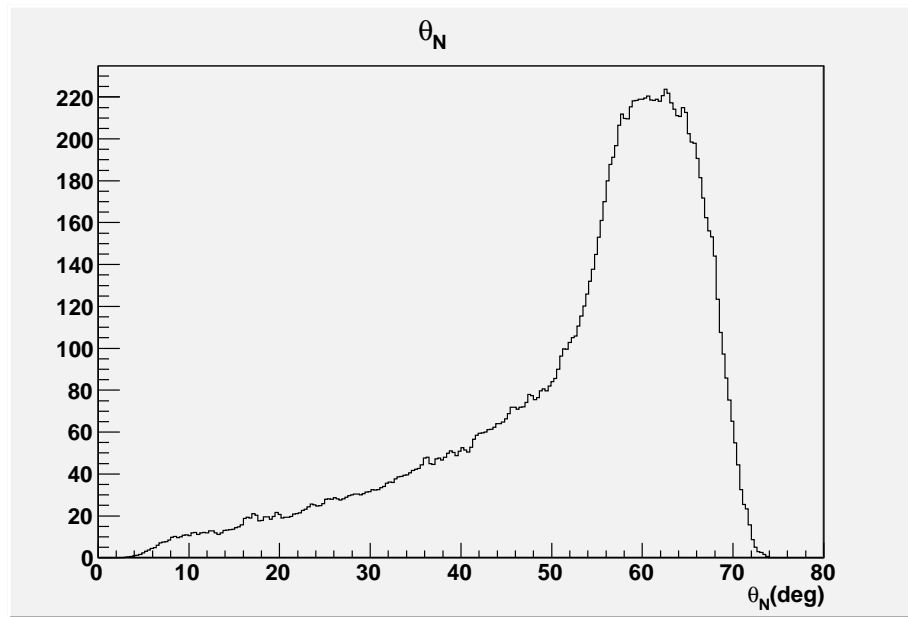


Figure 12: Neutron polar angle, for nDVCS events. Forward-CLAS12 acceptance cuts and physics cuts are included.

Substituting Eq. 6 in Eq. 5 one obtains:

$$p_e^\mu + p_n^\mu = p_{e'}^\mu + p_{n'}^\mu + p_\gamma^\mu. \quad (7)$$

Knowing the beam energy, if one identifies the final electron, photon and neutron and measures their angles and momenta, four unknowns (the components of the initial-neutron four vector) and four equations remain. The spectator proton kinematics can then be retrieved using the fact that, since the deuteron target is at rest:

$$\vec{p}_n^\mu + \vec{p}_p^\mu = 0, E_n + E_p = m_d. \quad (8)$$

As shown in the previous section, the electron and the DVCS photon will be emitted at small angles, and thus will be detected in the forward part of CLAS12 (with the photon either in the EC or in the IC), while the neutron will be emitted predominantly (for  $\sim 80\%$  of the events) at  $\theta > 40^\circ$  in the laboratory frame, with average momentum around 0.4 GeV/c. This points to the necessity to add a neutron detector (hereafter named Central Neutron detector, or CND) to the Central Detector of CLAS12, that in the present design has very limited detection efficiency for neutrons — they can be detected in the CTOF, with about 3% of efficiency.

With the aid of the CLAS12 FASTMC tool the requirements in terms of angular and momentum resolutions on the detected neutrons were determined. The kinematical variables of the scattered electron ( $e'$ ) and of the DVCS photon ( $\gamma$ ), computed by the nDVCS generator described in the previous section, were “smeared” using the values of resolutions produced by FASTMC. For the photons in the IC/Forward Tagger, the energy and angular resolutions were parametrized, respectively, as  $\sigma_{E_\gamma}/E_\gamma = 0.012/\sqrt{E}$ , which is the FT design goal [25], and  $\sigma_\theta = \frac{0.2}{\sqrt{510 \cdot E}}$  (taking the spatial angular resolution of the current IC —  $\sigma_x = \frac{0.2\text{cm}}{\sqrt{E}}$  — and assuming a target-IC distance of 510 cm).

The CND requirements were determined by looking at the missing mass of the  $e'n\gamma$  system, which is the only quantity one can “cut” on, in this detection topology, to ensure exclusivity for the nDVCS channel by minimizing the  $e'n\pi^0$  contamination. First of all, without applying any resolutions on the electron and photon kinematical variables, and varying instead the “smearing” on the neutron kinematic variables, it was proven that the resolution on the neutron momentum plays the major role in determining the width of  $MM(e'n\gamma)$ , while the effect of the angular resolutions is less important. This can be seen comparing Figs.13, 14 and 15, where the missing mass is computed varying, respectively, the neutron momentum, the polar and the azimuthal angle, while keeping the other two variables constant<sup>1</sup>. Varying either  $\sigma_\theta$  or  $\sigma_\phi$  by a factor 200 increases the width of  $MM(e'n\gamma)$  by only 5 MeV in absolute (corresponding to 33% more), while the same increase by a factor of 200 on the neutron momentum resolution  $\sigma_P/P$  worsens the resolution of the missing mass by a factor of 40 (its width passes from 2 MeV to 86 MeV).

Introducing the realistic resolutions on the electron and photon calculated by FASTMC, it appears (Figs. 16 and 17) that if the neutron momentum resolution is kept at the level of a few percent (below 10) its effect is negligible with respect to the other particles. In particular

---

<sup>1</sup>For these figures, the fixed values of the resolutions ( $\sigma_P/P = 4\%$ ,  $\sigma_\theta = 1.3^\circ$ ,  $\sigma_\phi = 3^\circ$ ) are the “realistic” ones, obtained from the GEMC simulation of the CND — see Section 6. However, as it will be explained in the following, the conclusions of the study do not depend on these particular values.

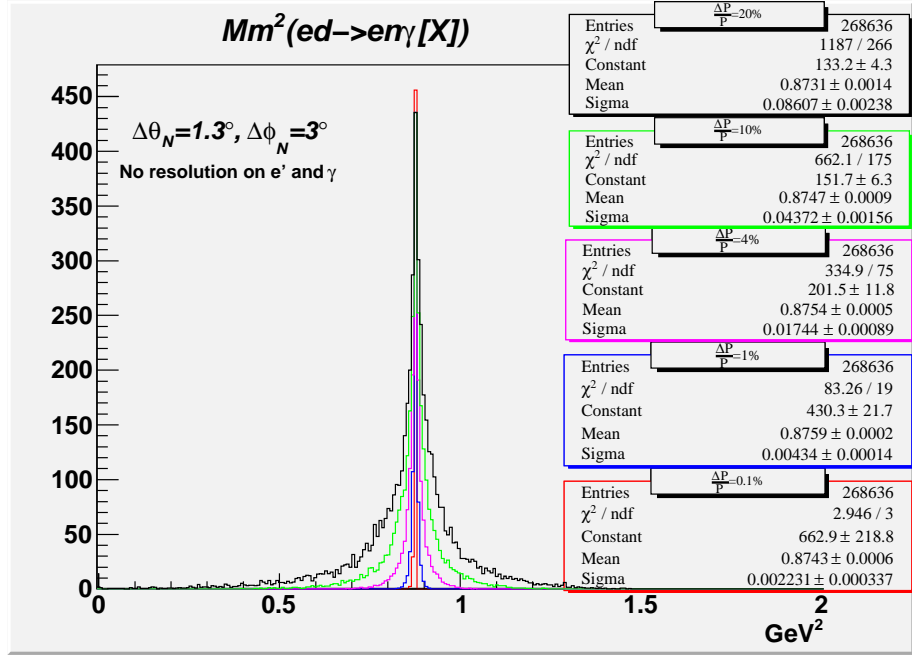


Figure 13: Missing mass squared of the  $e'n\gamma$  system, for the nDVCS channel, simulated with our event generator, assuming absolute precision on the photon and electron kinematic variables, fixing the neutron angular resolutions and varying the momentum resolution between 0.1% and 20%.

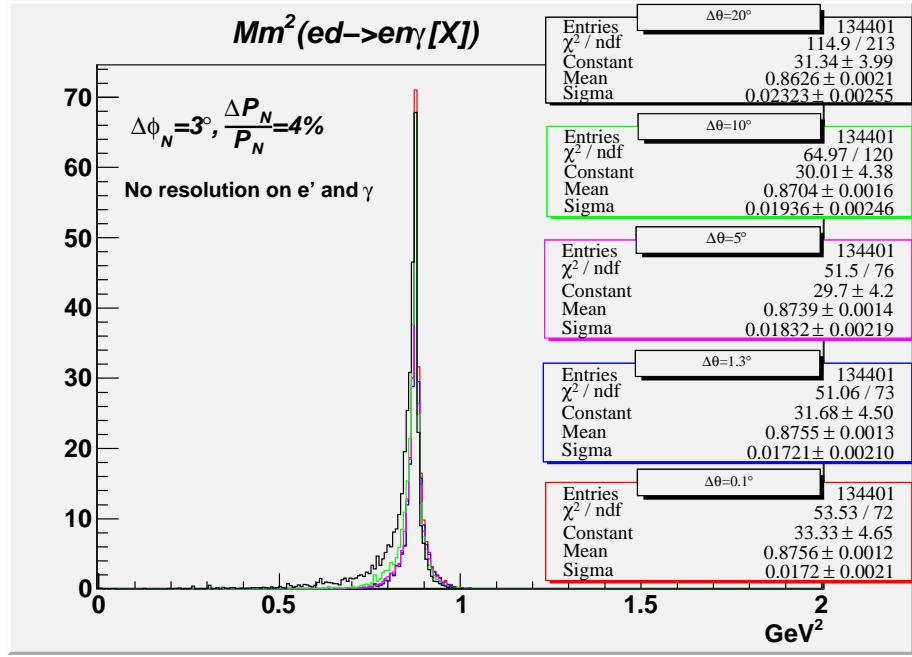


Figure 14: Missing mass squared of the  $e'n\gamma$  system, for the nDVCS channel, simulated with our event generator, assuming absolute precision on the photon and electron kinematic variables, fixing the neutron momentum and  $\phi$  resolutions and varying the  $\theta$  resolution between  $0.1^\circ$  and  $20^\circ$ .

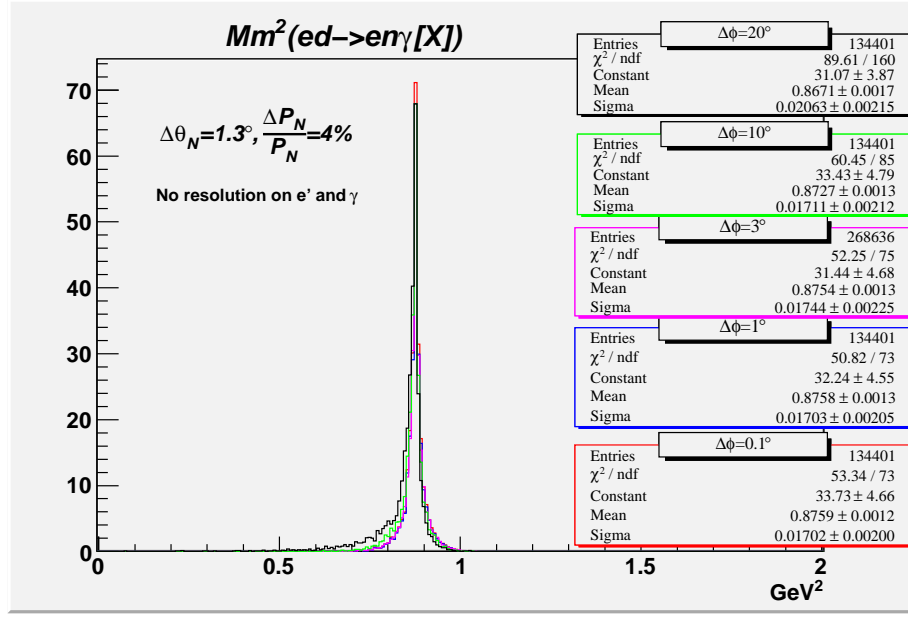


Figure 15: Missing mass squared of the  $e'n\gamma$  system, for the nDVCS channel, simulated with our event generator, assuming absolute precision on the photon and electron kinematic variables, fixing the neutron momentum and  $\theta$  resolutions and varying the  $\phi$  resolution between  $0.1^\circ$  and  $20^\circ$ .

(Fig. 17, green curve), the photon resolutions seem to be responsible of 80% of the width of the missing mass.

Therefore, considering that the detection capabilities of CLAS12 for electrons and high-energy photons are fixed, the requirements of the CND will be:

- good neutron identification capabilities for the kinematic range of interest ( $0.2 < p_n < 1.2 \text{ GeV}/c$ ,  $40^\circ < \theta_n < 80^\circ$ )
- neutron momentum resolution  $\sigma_P/P$  of the order of a few percent.

## 5 CND: R & D studies and final detector design

The available space in the Central Detector is limited by the presence of the CTOF and of the magnet, which leave about 10 cm free (Fig. 18). However, the CTOF can also be used to detect neutrons, adding a couple of percent of efficiency. The central tracker can also be very useful as a veto for charged particles. Finally, it is important to remind that there will be a surrounding magnetic field of 5 T, which complicates the issue of light collection.

About two years of simulations and R&D studies have been devoted to studying the various options for the CND and its possible photodetectors. After considering and then rejecting the option of a “spaghetti calorimeter” made of lead and scintillating fibers - it has a too high efficiency for photons as respect to neutrons - the retained design for the detector is a barrel of standard plastic scintillator bars of trapezoidal shape, all with their long sides parallel to the

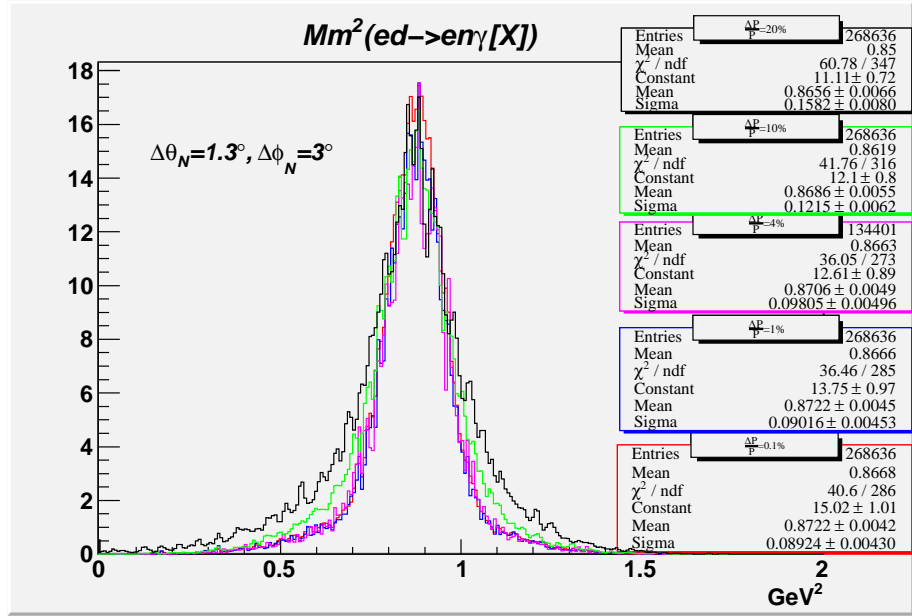


Figure 16: Missing mass squared of the  $e'n\gamma$  system, for the nDVCS channel, simulated with our event generator, assuming the nominal CLAS12 resolutions on the photon and electron kinematic variables, fixing the neutron  $\theta$  and  $\phi$  resolutions and varying the momentum resolution, between 0.1% and 20%.

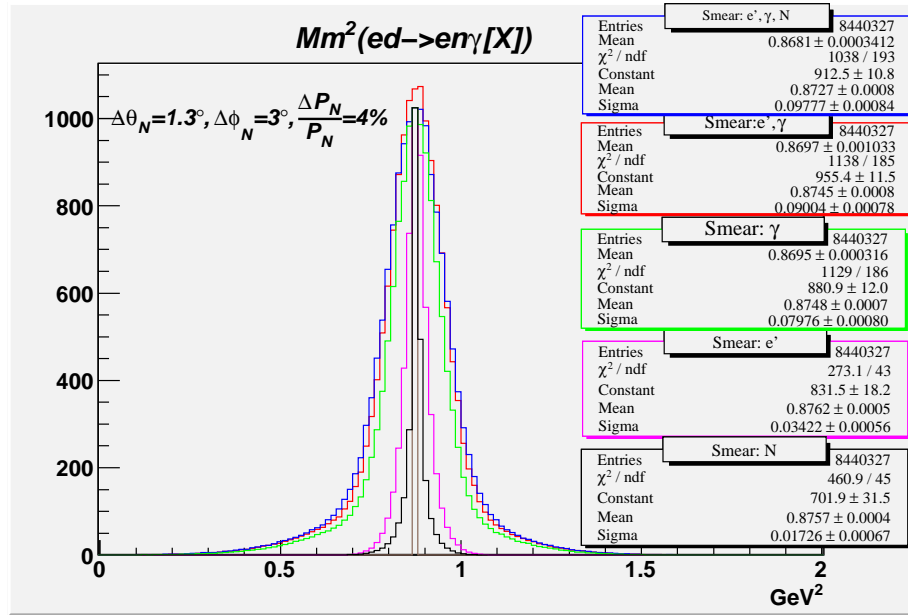


Figure 17: Missing mass squared of the  $e'n\gamma$  system, for the nDVCS channel, simulated with our event generator. The different colors correspond to different combinations of choices of particles being detected with absolute precision or with realistic resolutions.

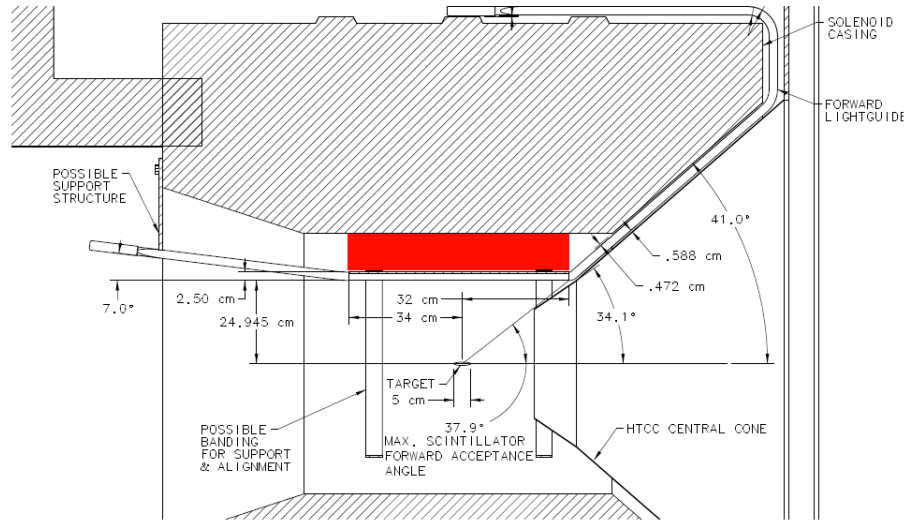


Figure 18: Drawing of the Central Detector: the red area represents the free space between the magnet and the CTOF.



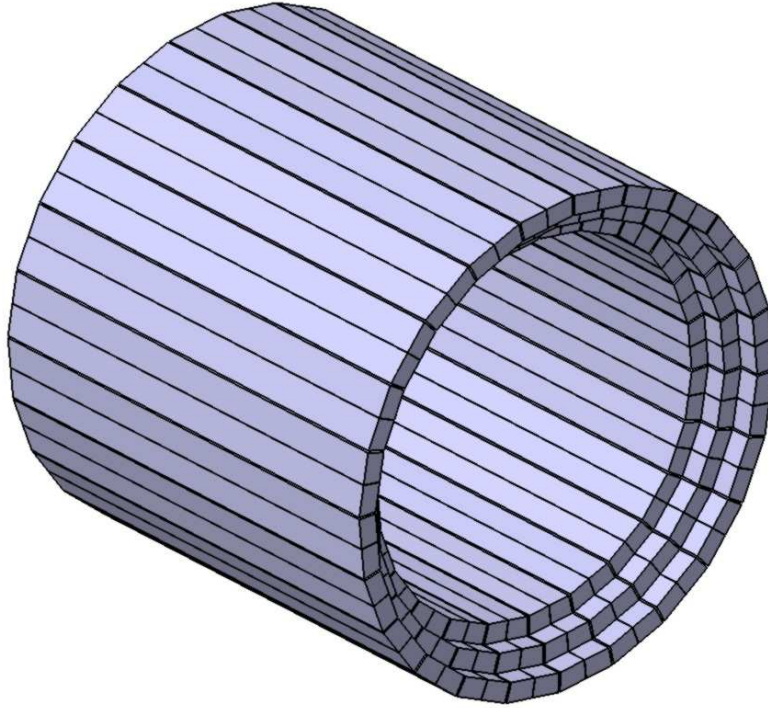


Figure 19: Geometry of the Central Neutron Detector. The current design consists of 3 radial layers each made by 48 trapezoidal scintillator paddles.

beam direction (Fig. 19). This geometry mimicks the one of the CTOF.

As stated in the previous section, one of the two requirements of the CND is good neutron identification capabilities. If the charged particles are vetoed by the central tracker, the only particles left that can be mistaken for neutrons are the photons. The only possible way to distinguish neutrons from photons using plastic scintillators is by measuring their time of flight. Early simulation studies [26] had shown that to ensure a good photon/neutron separation for the neutron momentum range of the nDVCS reaction the CND had to be equipped with photodetectors ensuring a time resolution of about 120-150 ps.

## 5.1 Summary of early R&D studies

The first part of our R&D studies had been focused on studying the timing performances of various magnetic-field resistant photodetectors, to be placed at the end of the scintillator bars, in the high-magnetic-field region of the Central Detector. In particular, measurements of time resolution with cosmic rays have been carried out using silicon photomultipliers (SiPMs), avalanche photo-diodes (APDs), and micro-channel-plate photomultipliers (MCP-PMTs). Neither of these devices has been retained. Two kinds of SiPMs were tested, the  $1 \times 1 \text{ mm}^2$  one and the  $3 \times 3 \text{ mm}^2$  one. The first was rejected because, due its small active surface,

it had a too small number of photoelectrons ( $\sim 1$ ) and hence yielded a too little time resolution<sup>2</sup> ( $\sim 1$  ns). The second was too noisy [36]. Matrices of SiPM (matrices 4x4 of 3x3mm<sup>2</sup> chips) have also been tested, giving promising results in terms of time performances [28], but they would require a very complex customized read-out electronics. The APD gave too high time resolution ( $\sigma_t \simeq 1.4$  ns), due to its big rise time. Good timing performances ( $\sigma_t \simeq 130$  ps) were obtained for the MCP-PMTs in the measurement without magnetic field, but when tested in a 5T magnetic field they displayed a too strong loss of gain [37]. Another reason to abandon the micro-channel-PMTs option was lifetime: we computed the expected flux of optical photons on the CND photodetectors due to electromagnetic background produced over the duration of our experiment, and it turned out to be more than a factor of magnitude higher than the limit, quoted in the literature [27], after which the quantum efficiency of the MCP-PMT drops [38].

## 5.2 Final design and performances

As the magnetic-field-resistant photodetectors proved to be not suited for the requirements of the CND, another solution was found: reading the light only at the backward end of each scintillator bar, with an ordinary PMT placed in the low-field region (Fig. 20) and connected to the bar by a 1-m-long bent light guide, while the front end of the bar is connected via a “u-turn” light guide to the neighboring guide. The light emitted at the front end of one scintillator is therefore fed through its neighboring paddle and read by the PMT connected to its end (Fig. 21).

The current plan for the detector segmentation is to have 48 azimuthal segments and 3 layers in the radial direction, for a total of 144 scintillator bars, coupled two-by-two (Fig. 19).

This configurations has been tested with measurements of time resolution with cosmic rays. A one-layer protototype has been built for this goal at the IPN Orsay (Fig. 22). It consist of two scintillator bars (BC408), each 66 cm long, 3 cm thick and 3.5 cm wide, joined at one end by a “u-turn” light guide and each connected at the other end to a 1-m-long bent light guide coupled to two ordinary PMTs (Hamamatsu R2083, at this stage<sup>3</sup>) (Fig. 23). A semi-circular shape for the u-turn light guide has been chosen, as it gave a lower loss of light than the other solution tested (triangular shape). For the wrapping, aluminum foil has been preferred to Mylar or VM2000 for its better timing performances and for its higher opacity, which minimizes “cross talk” between adjacent paddles [29]. In the middle of one of the two the bars, above and below it, are placed two smaller scintillators (1 cm thick, having 3x3 cm<sup>2</sup> of surface), each read by a fast PMT (Hamamatsu R2282), which are used to trigger the data acquisition and to insure that the position of the hit is known.

The output signals of the “top” (T) and “bottom” (B) trigger PMTs, as well the ones from the “direct” (D, the PMT of the bar where the hit takes place) and “neighbor” (N, the PMT of the adjacent bar) one, are discriminated and then fed to ADCs and TDCs. B and T are also averaged with a “mean-timer” (MT), which gives the start to the DAQ. The timing resolution

---

<sup>2</sup>The timing resolution of a photodetector coupled to a scintillator is in fact proportional to the inverse square root of the number of photoelectrons, so the more photons are collected the smaller the time resolution is.

<sup>3</sup>The PMT Hamamatsu R7997, costing about a third of R2083, will be tested in the next weeks.

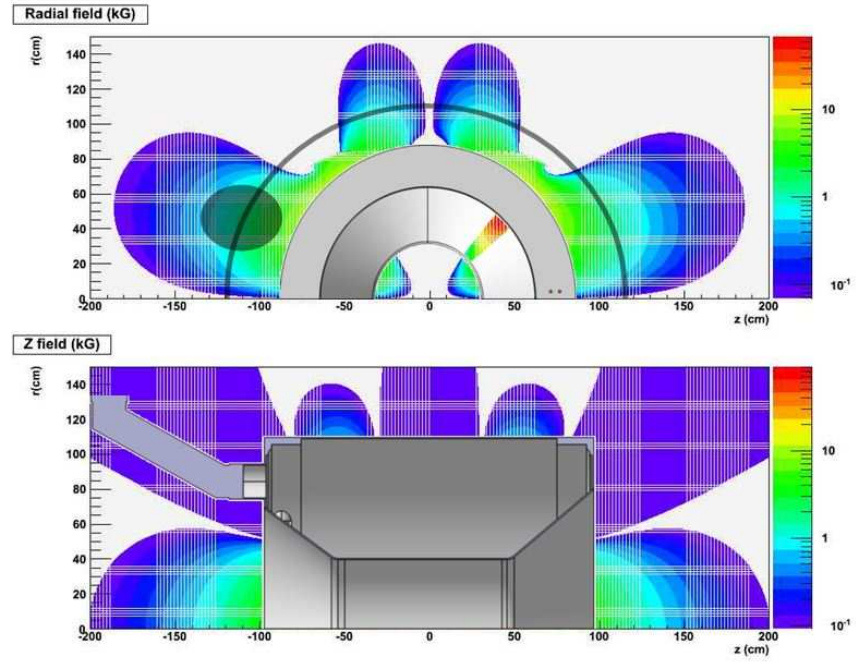


Figure 20: Magnetic field map for the Central Detector (radial component on the top, axial component on the bottom). The black line in the top plot shows the position of the PMTs of the Central Neutron Detector.

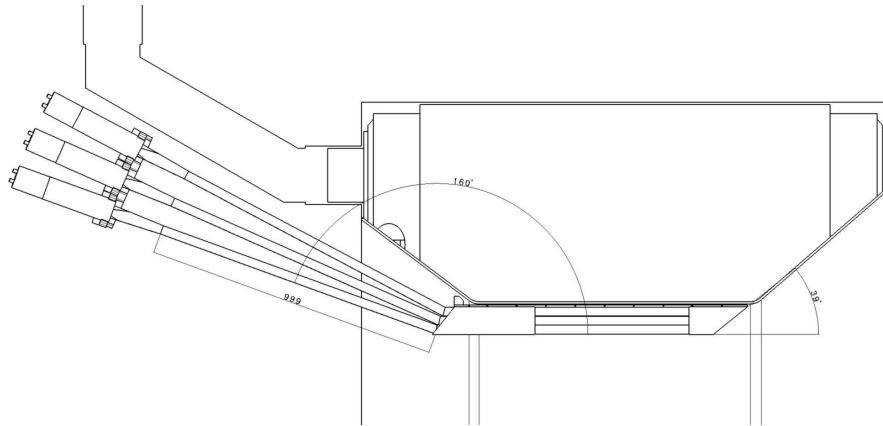


Figure 21: Drawing (side view) of the CND, placed into the solenoid magnet.

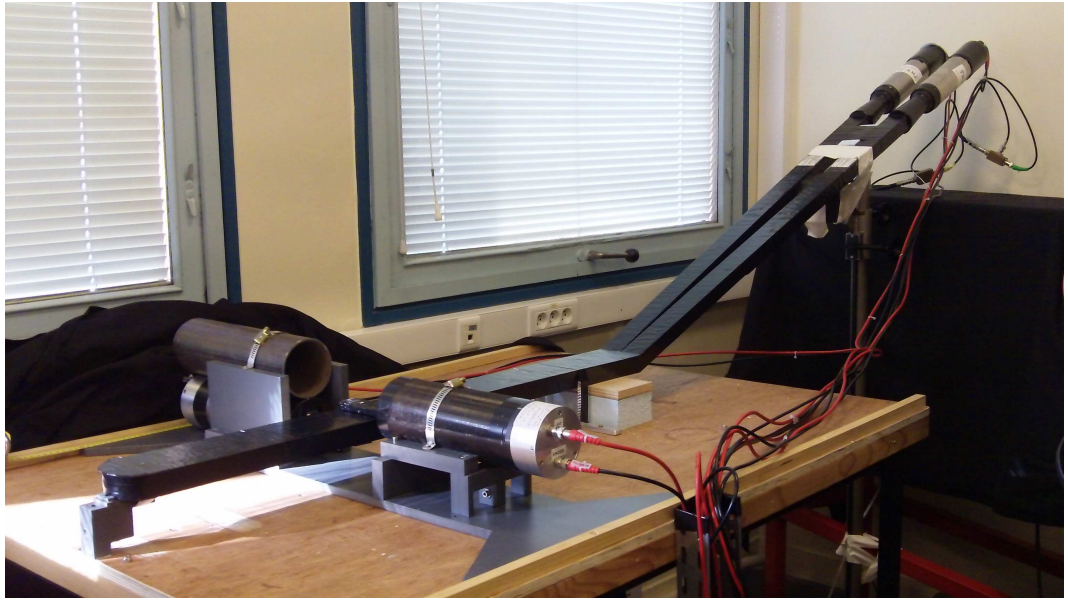


Figure 22: The one-layer prototype of the CND during the timing resolution measurements with cosmic rays carried out at Orsay.

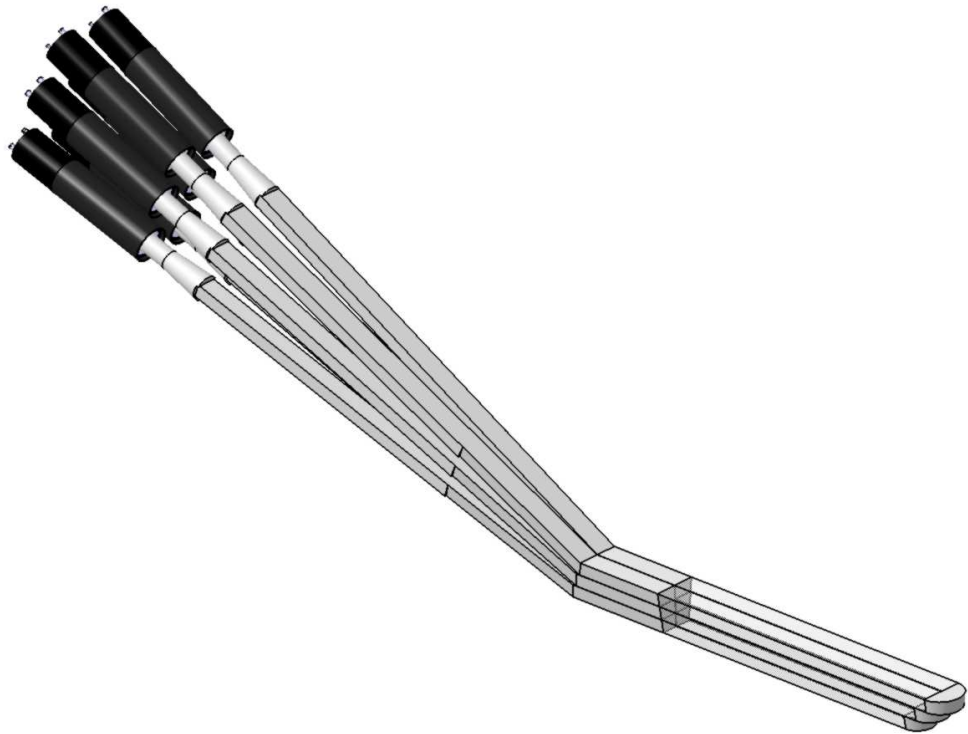


Figure 23: Drawing of the three-layer prototype of the CND, under construction.

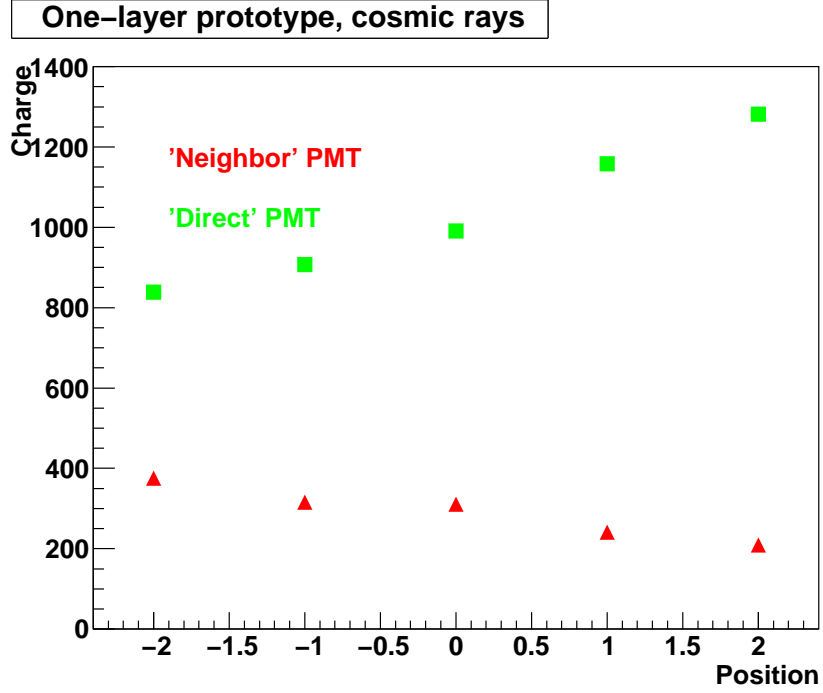


Figure 24: Charge collected by the two PMTs as a function of the position of the trigger for the one-layer prototype.

for the D or N PMTs is given by [29]:

$$\sigma_{D(N)} = \sqrt{\sigma_{D(N)-TRG}^2 - \sigma_{TRG}^2} \quad (9)$$

where  $\sigma_{D(N)-TRG}^2$  is the resolution of the time between the trigger and the Direct (Neighbor) signal, and

$$\sigma_{TRG} = t_{MT} - t_T = t_{MT} - t_B \quad (10)$$

is the time resolution of the trigger.

The results of the timing measurements with cosmic rays, performed varying the position of the trigger PMTs throughout the length of the scintillator bar, are shown in Figs.24 and 25. Position “0” corresponds to the center of the bar, “2” is close to the 2 PMTs, and “-2” is near the u-turn. From these figures, one can infer that:

- the “u-turn” brings about a factor of 2 of loss of collected charge
- the average timing resolutions for the two PMTs are:  $\sigma_D \simeq 120$  ps and  $\sigma_N \simeq 200$  ps.

These results are used in the simulation and the reconstruction for the CND — see next Section.

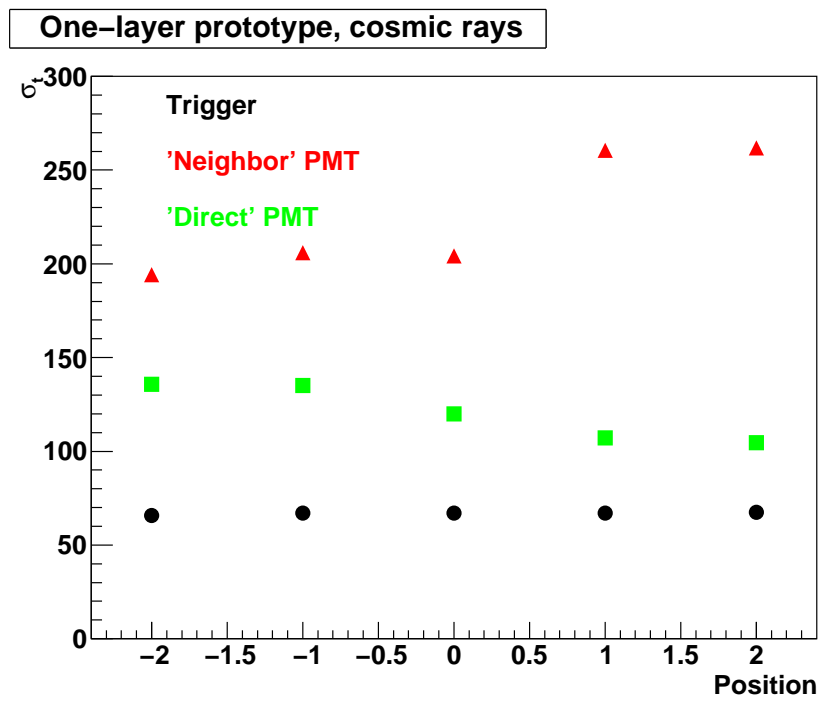


Figure 25: Time resolution of each PMT as a function of the position of the trigger for the one-layer prototype.

## 6 Simulation and reconstruction

In order to study the performances of this detector, its geometry has been added to the CLAS12 GEANT4-based simulation package, Gemc [30]. As respect to earlier studies [26] now the Birks effect, for which the amount of optical photon produced after a certain energy deposition in the scintillator depends on the particle losing that energy, and the hit digitization for the CND have been introduced in Gemc [32]. The timing resolution and the energy loss due to the u-turn geometry have been included in the simulation using the values measured in the cosmic-rays tests. More details on the digitization and on the hit and event reconstruction are explained in the Appendix (Sections 11.1 and 11.2). Simulations, which included all the components of the Central Detector, have been run to evaluate the efficiency of the CND for neutrons, its ability to discriminate between neutrons and photons, and its angular and momentum resolutions. Neutrons and photons of momenta varying between 0.1 and 1 GeV/c and having polar angles  $\theta$  varying between  $50^\circ$  and  $70^\circ$  have been generated at fixed azimuthal angle ( $\phi = 0^\circ$ ), pointing to the center of one of the scintillator bars. The results obtained with these simulations are described in Sections 6.1, 6.2 and 6.3.

### 6.1 Efficiency

The detection efficiency is defined here as the ratio between the number of events for which a “good hit” (see Section 11.2) was reconstructed in the correct azimuthal bin of the CND and the total number of neutrons generated. Several values of energy thresholds, between 1 and 5 MeV, have been tested. Figure 26 shows the efficiency as a function of the threshold, for neutrons with momentum of 0.4 GeV/c. The different colors correspond to 3 different values of the neutron polar angle,  $\theta_n$ . The efficiency, which decreases with increasing threshold, ranges between 12% at the lowest thresholds and 7% at the highest ones. Figure 28 shows instead the efficiency as a function of the momentum of the neutron, at a fixed energy threshold of 2 MeV, and for different values of  $\theta_n$ . All of these plots have been done with a cut rejecting hits with time of flight larger than 8 ns. This cut has been applied to suppress the events in which the neutrons interact in the magnet (without depositing energy in the CND) and rescatter or produce secondary particles hitting the CND at a later time, compromising the PID and the determination of the angles. This cut, along with a choice of threshold on the deposited energy of a few MeV (2 is the value chosen at the present stage), is effective in removing these secondary hits (more details on this aspect can be found at [31] and [32]).

### 6.2 Particle Identification

Since the charged particles passing through the CND will be vetoed by the Central Tracker, the only particles that could be mistaken for neutrons in the CND are the photons. The efficiency of the CND for photons has been estimated by simulations, and it is comparable to the one for neutrons (of the order of 10%, see Fig. 29). Neutrons can be discriminated from photons by means of their  $\beta$ .

Therefore, the  $\beta$  distributions that can be obtained with the CND for neutrons and photons have been studied with the aid of the Gemc simulation. After choosing as “good hit” as described above,  $\beta$  is computed as

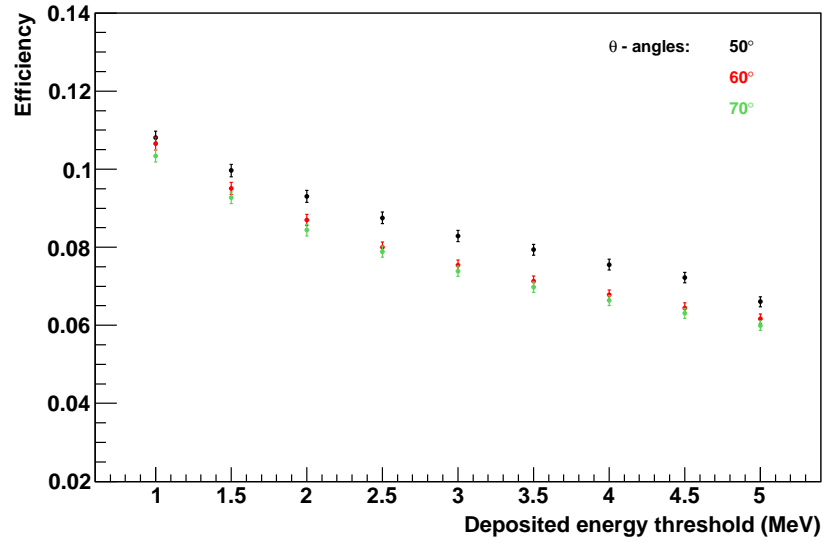


Figure 26: Efficiency for the detection of neutrons having 0.4 GeV/c of momentum, as a function of the threshold on the deposited energy. The efficiency is shown for 3 different values of  $\theta_n$ , between 50° and 90°.

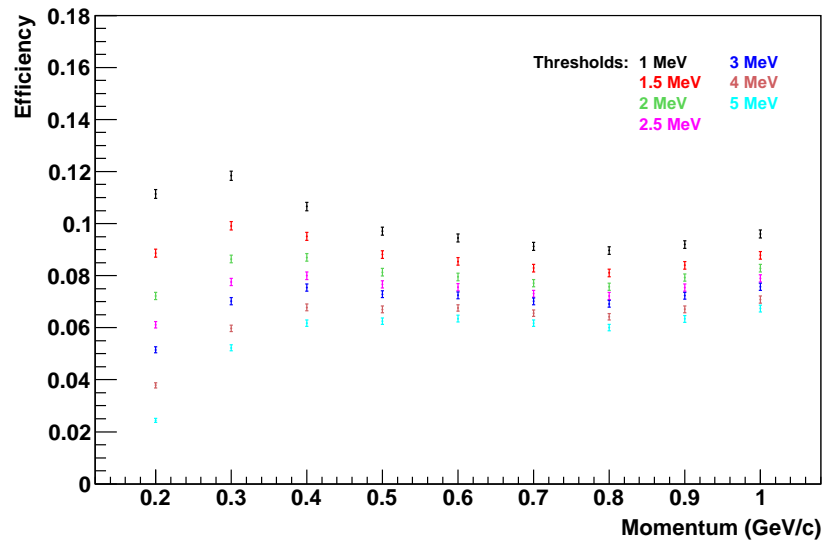


Figure 27: Efficiency for the detection of neutrons emitted at 60°, as a function of momentum, for 7 different values of the threshold on the deposited energy, from 1 to 5 MeV.



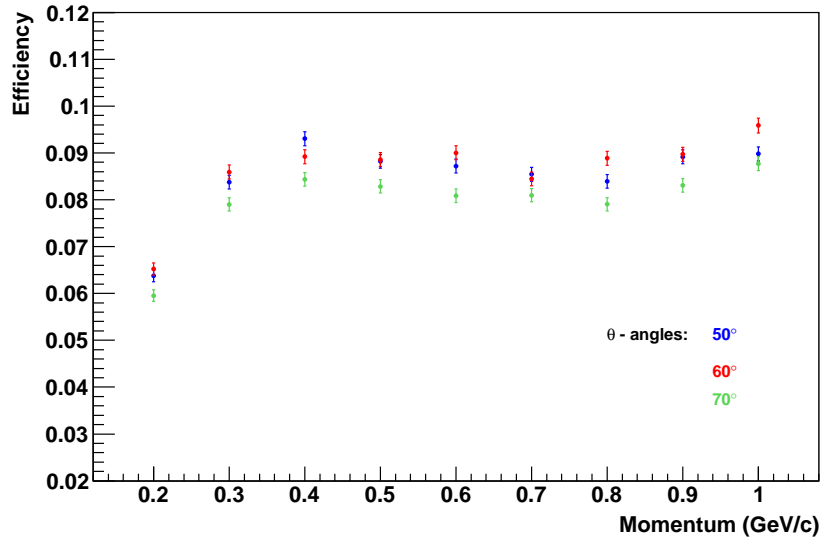


Figure 28: Efficiency for the detection of neutrons, as a function of neutron momentum, for a 2-MeV threshold on the deposited energy. The efficiency is shown for three different values of  $\theta_n$ , between  $50^\circ$  and  $70^\circ$ .

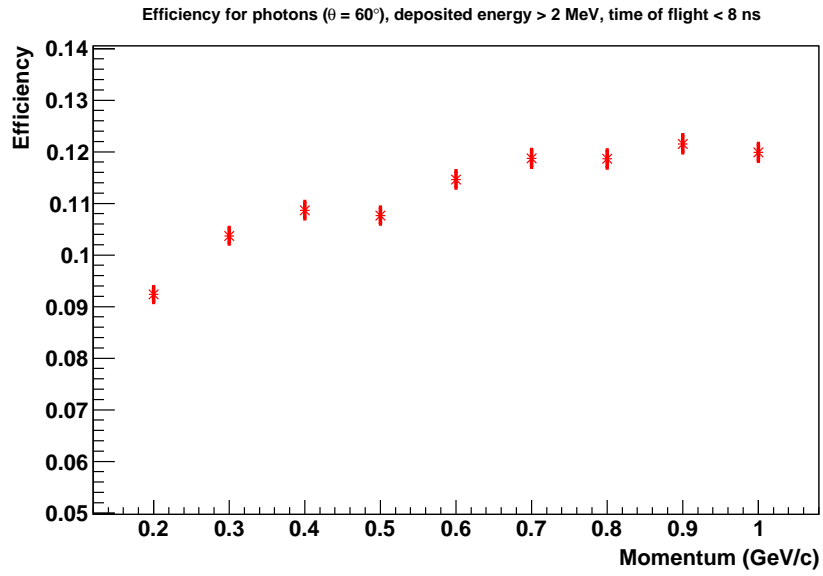


Figure 29: Efficiency for the detection of photons, as a function of photon momentum, for a 2-MeV threshold on the deposited energy. The efficiency is shown for  $\theta_\gamma = 60^\circ$

$$\beta = \frac{l}{TOF_{true} \cdot c}, \quad (11)$$

where

$$l = \sqrt{h^2 + z_{ave}^2}, \quad (12)$$

$h$  is the distance from the vertex to the middle of the layer where the hit took place,  $TOF_{true}$  is the reconstructed time of flight and  $z_{ave}$  is the reconstructed position of the hit (see Appendix 11.2 for more details on how these last two quantities are obtained).

Figure 30 shows the comparison, for each of the 3 radial layers and integrating over the azimuthal angle, between the  $\beta$  distributions obtained for neutrons of various momenta (0.2, 0.4, 0.7 and 1 GeV/c) and for 1-GeV photons (in black). All particles in this plot are emitted at  $\theta = 60^\circ$ . Neutrons of momentum of 0.9-1 GeV/c can be taken as photons, as their  $\beta$  distributions begin to overlap, while for lower momenta (which correspond to the range of interest for nDVCS) the n/ $\gamma$  separation is clear. This is evident also from Fig. 31, where the error bars correspond actually to  $3\sigma$ , where  $\sigma$  is the gaussian width of each  $\beta$  distribution.

### 6.3 Angular and momentum resolutions

The resolutions on the polar angle  $\theta$  of the neutron that can be obtained with the CND are strongly linked to its TOF resolution. The angle  $\theta$  is in fact given by

$$\theta = (180/\pi) \cdot \arccos\left(\frac{z_{ave}}{l}\right) \quad (13)$$

where  $l$  and  $z_{ave}$ , that were defined earlier, both depend on the time measurement. Using the value  $A = 0.24 \text{ ns} \cdot \text{MeV}^{-1/2}$  for the gaussian smearing on the timing, the  $\theta$  resolution was studied with Gemc, as a function of neutron momentum. The results are shown in Fig. 32, where the angular resolution  $\sigma_\theta$ , obtained via gaussian fits of the simulated  $\theta$  distributions, is plotted as a function of  $\theta$ , for a particular value of neutron momentum (0.4 GeV/c).  $\sigma_\theta$  increases slightly with the angle and also is fairly constant a function of neutron momentum, and its value is between  $1.5^\circ$  and  $3.5^\circ$ .

The resolution on the azimuthal angle is directly connected to the total number of scintillator bars along  $\phi$ . In fact, the bin size  $\Delta\phi$  is given by

$$\Delta\phi = \frac{360^\circ}{N} = 7.5^\circ \quad (14)$$

where  $N_{paddle}$  is the ID number of the paddle where the hit took place, and  $N$  is the total number of paddles in  $\phi$  (48 for the current design of the CND).  $\sigma_\phi$  can be taken as half of  $\Delta\phi$ , therefore  $3.75^\circ$ .

The resolution on the neutron momentum, which can be obtained knowing  $\beta$  and having performed the particle identification, is also strictly connected to the TOF resolution. Figure 33 shows the momentum resolution  $\sigma_p/p$  as a function of momentum for neutrons emitted with  $\theta = 60^\circ$ : it increases with increasing momentum, and ranges between 4% and 11%. No appreciable variations of momentum resolution are observed by varying the neutron polar angle.

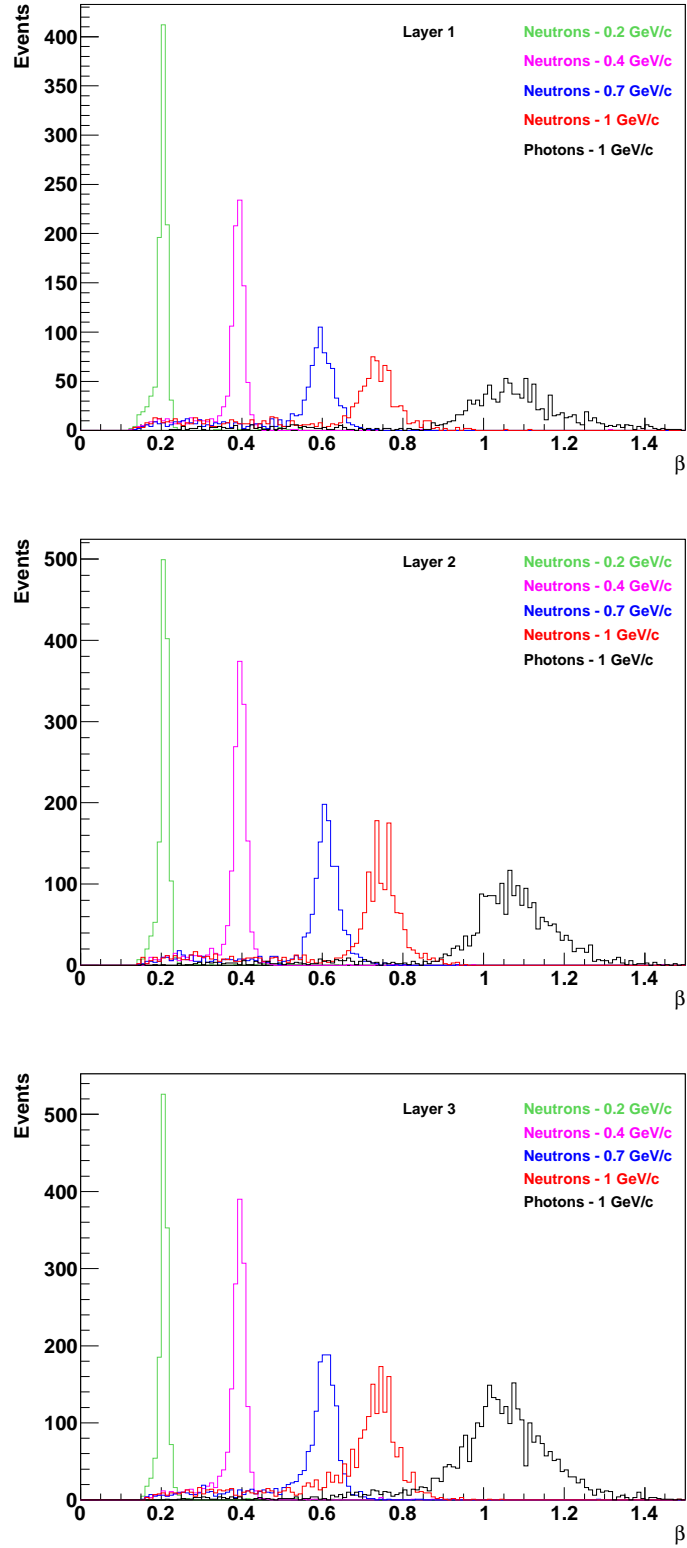


Figure 30:  $\beta$  distributions for neutrons with  $p_n = 0.2$  GeV/c (green),  $p_n = 0.4$  GeV/c (purple),  $p_n = 0.7$  GeV/c (blue),  $p_n = 1$  GeV/c (red), and photons with  $E = 1$  GeV. Each box shows the results for one of the three radial layers that compose the CND (the innermost is on the top, the outermost is on the bottom). The threshold on the deposited energy is 2 MeV. The plots show all hits, integrated over  $\phi$ . Equal neutron and photon yields have been assumed here.

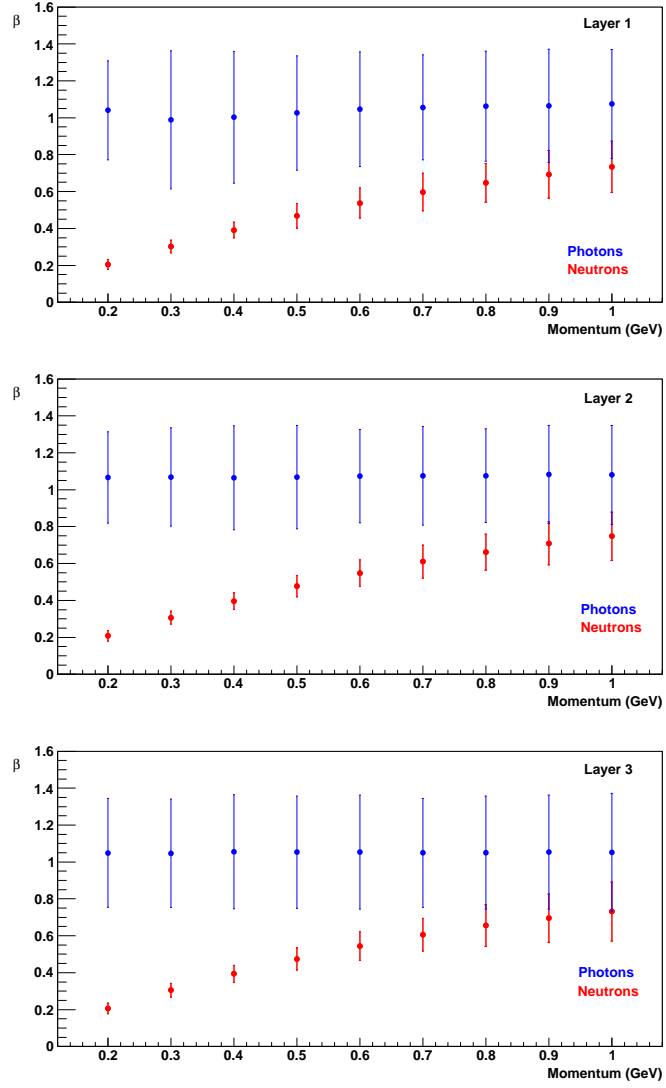


Figure 31:  $\beta$  versus momentum for neutrons (red) and photons (blue) with momenta between 0.2 and 1 GeV. The error bars are defined as  $3\sigma$ , where  $\sigma$  is the fitted width of each  $\beta$  peak. The threshold on the deposited energy is 2 MeV.

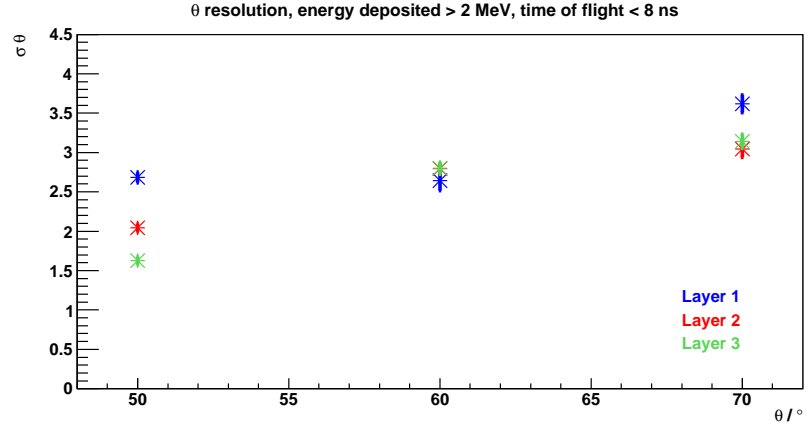


Figure 32: Angular resolution  $\sigma_\theta$  as a function of  $\theta$  for neutrons of momentum 0.4 GeV/c, for a 2-MeV threshold on the deposited energy. The three colors of the points correspond to the three radial layers of the CND.

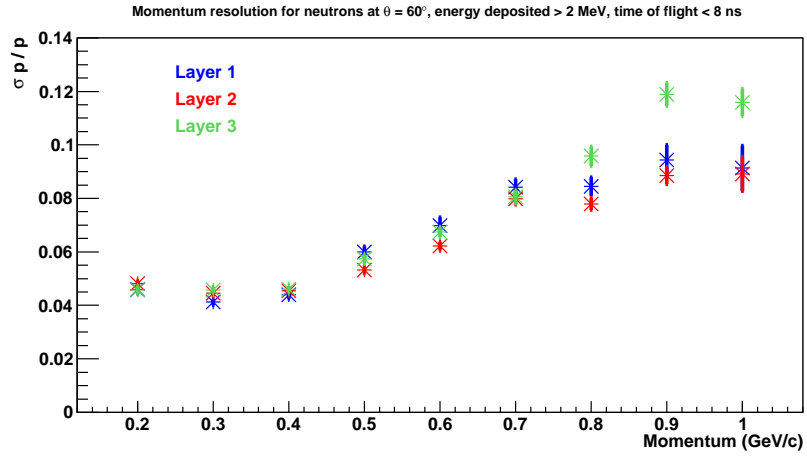


Figure 33: Momentum resolution  $\sigma_p/p$  as a function of  $p$  for neutrons having  $\theta = 60^\circ$ , for a 2-MeV threshold on the deposited energy. The three colors of the points correspond to the three radial layers of the CND.

## 7 Count-rate estimate

The nDVCS final state will be reconstructed by detecting the scattered electron and the DVCS/BH photon in the forward part of CLAS12 and the recoil neutron mostly in the CND, as very few neutrons are emitted in the forward direction with enough momentum to be detected in EC with appreciable efficiency. The expected number of reconstructed events for nDVCS has been calculated, as a function of the kinematics, with the event generator described in Section 3. The forward-CLAS12 fiducial cuts have been included, and an overall 10% neutron-detection efficiency (keeping into account the few percents of efficiency that can be obtained with the CTOF) for neutrons with  $\theta > 40^\circ$  has been assumed (at this stage, the forward CLAS12 neutron-detection efficiency has been neglected). The electron and photon-detection efficiencies for the Forward Detector have been assumed to be 100%, within the fiducial cuts. The calculation has been done for a luminosity  $L = 10^{35} \text{ cm}^{-2}\text{s}^{-1}$  and for 80 days of running time. A 4-dimensional grid of 2160 bins (6 bins in  $Q^2$  and  $-t$ , 5 bins in  $x_B$ , 12 bins in  $\phi$ ) has been adopted. The number of events, for each 4-dimensional bin ( $Q^2$ ,  $x_B$ ,  $t$  and  $\phi$ ), has been computed as:

$$N = \frac{d\sigma}{dQ^2 dx_B dt d\phi} \cdot \Delta t \cdot \Delta Q^2 \cdot \Delta x_B \cdot \Delta \phi \cdot L \cdot T \cdot R_{acc} \cdot Eff, \quad (15)$$

where  $\frac{d\sigma}{dQ^2 dx_B dt d\phi}$  is the 4-fold differential cross section,  $T$  is the running time,  $L$  the luminosity,  $R_{acc}$  is a bin-by-bin acceptance factor and  $Eff$  is the neutron-detection efficiency.

In Table 7 the expected 4-fold differential cross sections, the 4-dimensional acceptance and the corresponding number of events are listed for one particular kinematic bin ( $\langle t \rangle = -0.4 \text{ GeV}^2$ ,  $\langle Q^2 \rangle = 2.5 \text{ GeV}^2$ ,  $\langle x_B \rangle = 0.14$ ) as a function of  $\phi$ . These yields correspond to statistical errors on the cross section between 2% and 10%. The same quantities are shown in Fig. 35. The error on the beam-spin asymmetry will then depend on the values of the BSA itself ( $A$ ) and of the beam polarization ( $P$ ), through the formula:

$$\sigma_A = \frac{1}{P} \cdot \frac{\sqrt{(1 - P \cdot A)^2}}{\sqrt{N}}. \quad (16)$$

Figure 34 shows the expected accuracy on the nDVCS beam-spin asymmetry, computed using the VGG model and assuming  $J_u = .3$  and  $J_d = .1$ , for the kinematic bin of Table 7. The error bars are at most of the order of 20% in relative.

By summing on all the count rates obtained for the full grid of bins, we can have an estimate of the total expected count rate. Overall, roughly 25 million of nDVCS events are expected to be collected over the full kinematic range of interest, corresponding to an integrated rate of 4 Hz for the 80 days of running time.

## 8 $en\pi^0(p)$ background

Once the events containing one electron, one neutron and one photon are selected, the nDVCS/BH final state can be isolated by cutting on the  $en\gamma$  missing mass. However, due to the finite resolutions on the various kinematic variables measured, the final event sample will still

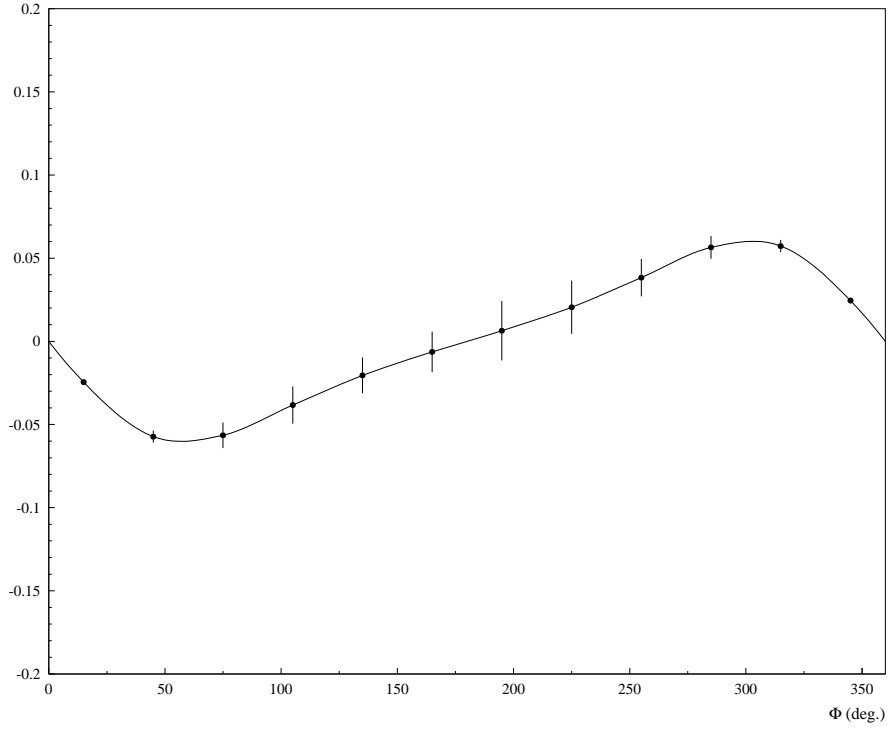


Figure 34: Beam-spin asymmetry for nDVCS as predicted by the VGG model (for  $J_u = .3$  and  $J_d = .1$ ), plotted as a function of  $\phi$  for the kinematic bin  $t = -0.4 \text{ GeV}^2$ ,  $Q^2 = 2.5 \text{ GeV}^2$ ,  $x_B = 0.14$ . The error bars reflect the expected uncertainties for our experiment, corresponding to 80 hours of beam time at a luminosity of  $10^{35}$ .

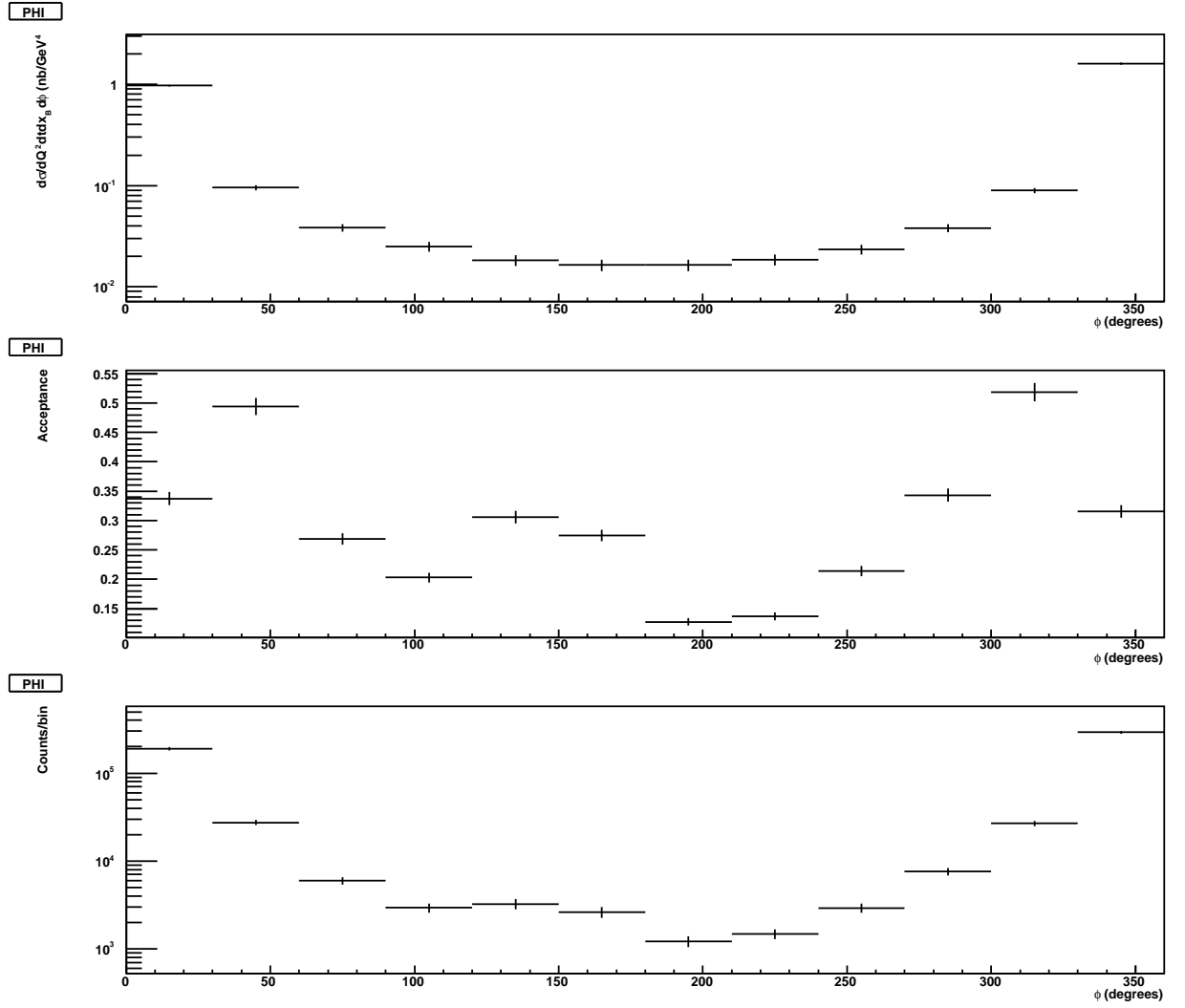


Figure 35: Top: cross section for nDVCS. Middle: acceptance for the nDVCS channel, including only CLAS12, computed with our event generator + FASTMC. Bottom: expected count rate for 80 days of beam time. All three plots are produced for the kinematic bin of Table 7.



Table 1: Expected 4-fold differential cross sections, 4-dimensional acceptance and number of events for nDVCS with CLAS12 and the CND, as a function of  $\phi$ .  $\langle t \rangle = -0.4 \text{ GeV}^2$ ,  $\langle Q^2 \rangle = 2.5 \text{ GeV}^2$ ,  $\langle x_B \rangle = 0.14$ ,  $\Delta\phi = 30^\circ$ ,  $\Delta Q^2 = 1 \text{ GeV}^2$ ,  $\Delta x_B = 0.08$ ,  $\Delta t = 0.2 \text{ GeV}^2$ . The calculation was done for a luminosity  $L = 10^{35} \text{ cm}^{-2}\text{s}^{-1}$  and for 80 days of running time.

$\phi(^{\circ})$	$\frac{d\sigma}{dQ^2 dx_B dt d\phi}(\text{nb/GeV}^4)$	Acceptance	Nb events
15	0.9702	3.4%	189437
45	0.0958	4.9%	27417
75	0.0384	2.7%	5982
105	0.0249	2.0%	2937
135	0.0183	3.1%	3241
165	0.0165	2.7%	2616
195	0.0164	1.2%	1217
225	0.0186	1.3%	1480
255	0.0234	2.1%	2908
285	0.0382	3.4%	7595
315	0.0895	5.2%	26878
345	1.599	3.1%	292046

be contaminated by  $en\gamma$  events coming from the  $en\pi^0(p)$  channel, where one photon from the  $\pi^0$  decay is detected in the forward part of CLAS12 while the other escapes detection. This contamination will be evaluated - and subtracted - as done in previous DVCS CLAS analyses [10], by extracting exclusively  $en\pi^0(p)$  events from the data, and using Monte Carlo simulations to evaluate the ratio of acceptances of  $\pi^0$  events with 1 and 2 photons detected. The final number of nDVCS events will be obtained as:

$$N_{DVCS} = N_{en\gamma X} - N_{\pi^0}^{data} \cdot \frac{N_{\pi^0 1\gamma}^{MC}}{N_{\pi^0}^{MC}} \quad (17)$$

With the aid of our event generators, we have estimated the expected level of  $\pi^0$  contamination for the proposed experiment. Both the angular and momentum resolutions for neutrons obtained with the simulation of the CND, as well as the resolutions on electrons and photons coming from CLAS12 FAST-MC, have been implemented in the nDVCS and  $e(p)n\pi^0$  event generators. Fiducial cuts have been applied on all the three final-state particles. For the  $en\pi^0(p)$  cross section, we have used the model for exclusive  $\pi^0$  electroproduction on the nucleon developed by J.M. Laget [39]. This model is based on Regge theory with the inclusion of rescattering processes. It provides estimations of cross sections which are in agreement with the ones measured by the JLab collaborations of Hall A [40] and Hall B [41] on the proton. In this model, in the kinematical domain explored in this proposal, the exclusive  $\pi^0$  cross section on the proton is basically equal to the one on the neutron.

Figure 36 shows, superimposed, the  $e'n_{\text{gamma}}$  missing mass squared for nDVCS (red) and  $e(p)n\pi^0$  (black) events, produced by our generators, integrated over the full kinematic range of interest. Applying the cut  $MM^2 < 1 \text{ GeV}^2$  the  $\pi^0$  contamination is around 10%. (NEED

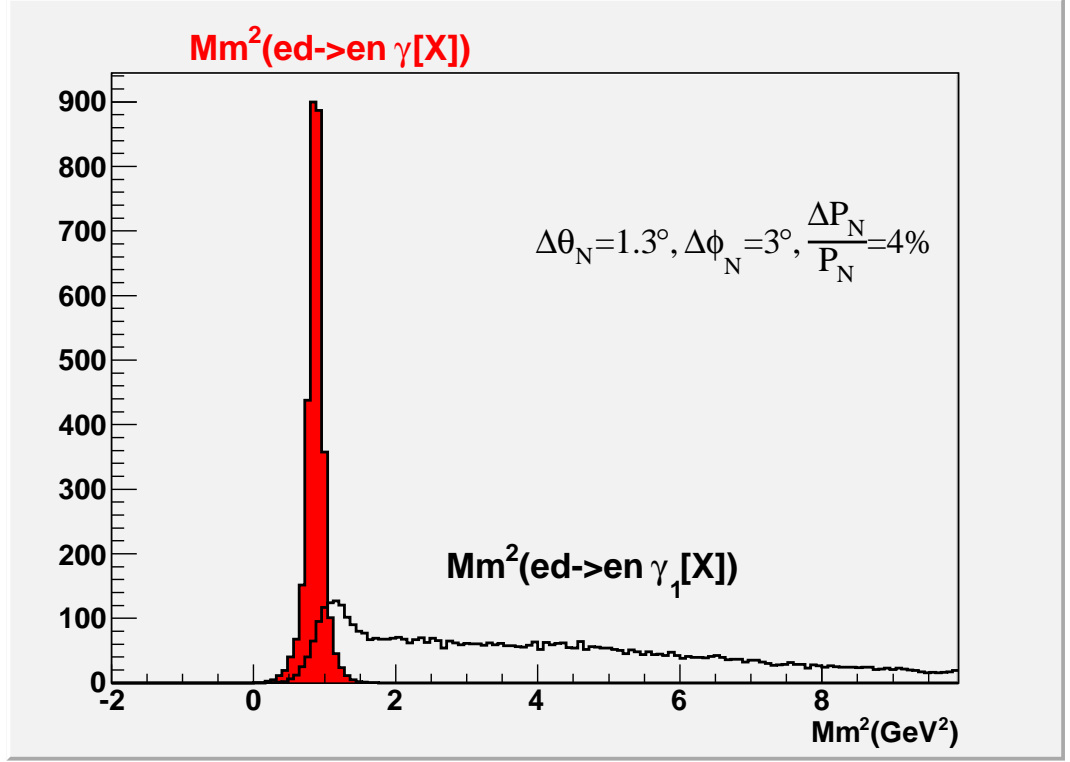


Figure 36: Missing mass of the  $e'n\gamma$  system, for the nDVCS channel (in red), and the  $ed \rightarrow e'n\pi^0(p)$  channel (in black), both simulated with our event generator. “Realistic” CLAS12 and CND resolutions are applied.

TO EVALUATE EXACT FIGURE, and maybe also its  $\phi$  dependence - NEXT WEEK)

## 9 Backgrounds on the CND

As described earlier, photons are the main source of background for the CND, as they can be mistaken for neutrons. Charged particles, instead, will be vetoed by the Central Tracker. Two kinds of photons can contribute to this background: physical events, for instance  $\pi^0$  production where one of the two decay photons is emitted at backwards angles, and photons produced by electromagnetic reactions of the electron beam in the target.

### 9.1 Physics background

An estimate of the hadronic background has been deduced, using the clasDIS event generator (based upon PYTHIA). The background events that could mimic a nDVCS event are those having:

- one energetic photon ( $E_\gamma > 1$  GeV) in forward direction

- one photon in the central detector.

For these kinds of events, the estimated rate at full luminosity ( $10^{35} \text{ cm}^{-2}\text{s}^{-1}$ ) in the DIS kinematics is 1.2 KHz. If one also requires the missing mass for the  $e\gamma$  system (calculated on a neutron target) to be below  $1 \text{ GeV}/c^2$ , the rate drops to 5 Hz. Assuming a 60% acceptance for the electrons and for the photons detected in the forward detector, the rate goes down to about 2 Hz. Finally, keeping into account 10-15% of efficiency of the CND for photons, the resulting rate, that can be directly compared to the neutron one, reported in the previous Section, is about 0.3 Hz. The assumption of equal rates, made when studying the photon/neutron separation capabilities of the CND (see Section 6.2), is therefore a conservative one. Under this assumption, it was shown that in the CND photons can be distinguished from neutrons provided that the latter have momenta below  $1 \text{ GeV}$ . This corresponds to the majority of the nDVCS events, for which neutrons mostly emitted with momentum around  $0.4 \text{ GeV}$ .

## 9.2 Electromagnetic background - THE MC JOBS FOR THIS SECTION ARE STILL RUNNING, NUMBERS TO BE UPDATED IN THE NEXT DAYS

In order to evaluate the effects of the electromagnetic background on the Central Neutron Detector, in particular to estimate the actual rates seen by the CND due to the background and the energy and timing distributions of the background hits, Gemc simulations have been run in the following conditions [43]: the primary electron has been generated going forward (to simulate the real hadronic event), plus roughly 60000 other electrons have been thrown, distributed in a 124 ns window in bunches 2 ns apart, originating 10 cm upstream the target. These electrons then interact with the target itself, producing an electromagnetic background hitting the neutron detector. 60000 is approximately the number of beam electrons that would pass through the target in a 124 ns time window at the nominal CLAS12 luminosity. 124 ns is the typical time window of the DAQ expected for CLAS12, which corresponds to one event in CLAS12. Figure 37, produced with the interactive version of Gemc, shows one typical “background event” in the Central Detector: the red tracks correspond to negatively charged particles (electrons) while the green ones are neutrals (mostly photons). The hits in the CND, in green/blue-ish, are mainly due to photons.

The output of these simulations has been analyzed using the event-reconstruction algorithm adopted to reconstruct neutrons in the CND.

In general, the energy deposited in the CND by the electromagnetic-background photons is quite small, as it can be seen in Fig. 38, where the energy deposition in the whole CND is plotted. These photons tend to release their energy mainly in the first radial layers of the CND, as shown in Figure 39. If no threshold on the deposited energy or timing cuts are applied, the total rate on the CND due to the electromagnetic background is about ? GHz.

Cutting on the deposited energy at  $2 \text{ MeV}$ , the value which has been chosen to optimize the PID and angular resolution (Section 6.1), the rate drops to a few KHz. The hit multiplicity per event is roughly 1, and almost all of the surviving events have  $\beta < 0.1$ . Considering that  $\beta = 0.1$  corresponds to a neutron momentum of less than  $0.1 \text{ GeV}/c^2$ , which is below the typical cut that needs to be applied to remove neutron-spectator events (around  $0.15 \text{ GeV}/c^2$ ), the greatest majority of these kinds of background events will be completely removed in the data

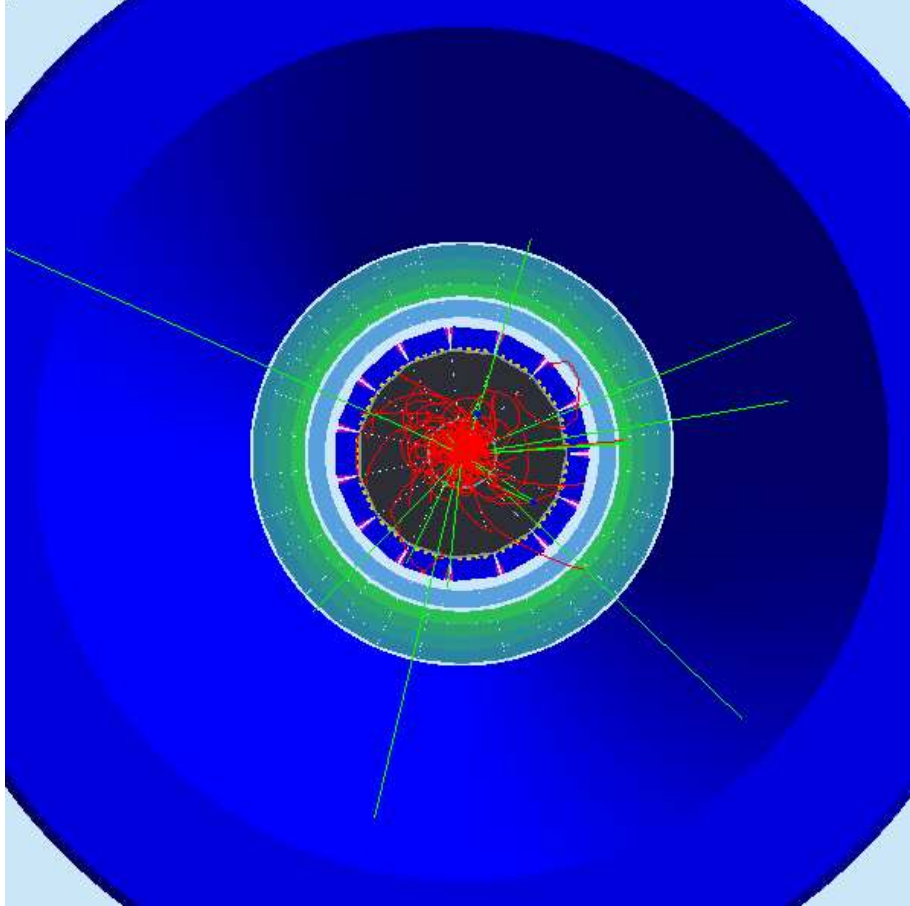


Figure 37: View (from the beam's perspective) of the Central Detector, for one simulated “background event”. Red tracks correspond to negatively charged particles, green tracks correspond to neutrals. This picture has been obtained for a luminosity  $L = 10^{33} \text{ cm}^{-2}\text{s}^{-1}$ , corresponding to 1/100 of the nominal luminosity, for practical reasons related to the graphical interface.

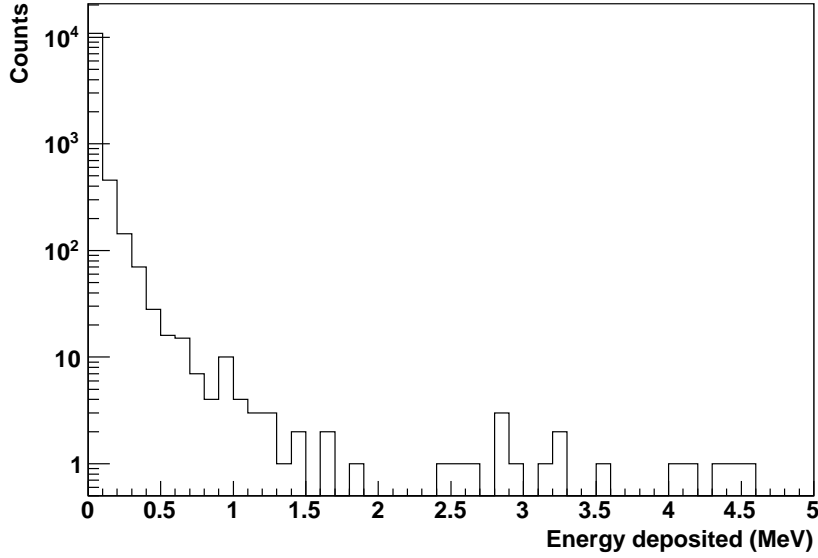


Figure 38: Distribution of the energy deposit in the CND, integrated over all the azimuthal and radial bins, of the hits coming from the generated electromagnetic background. The majority of the events correspond to an energy release below 1 MeV.

analysis. The few remaining hits can mimic a fake nDVCS event by accidental coincidence with hadronic events where an electron and photon are detected in the forward part of CLAS12. Assuming for example a rate for such events of the order of 1 KHz, the accidental coincidence rate is of the order of 0.5 Hz and is therefore negligible with respect to the physics background discussed in the previous section.

## 10 Summary and conclusions

The strong sensitivity to the GPD  $E$  of the beam-spin asymmetry for DVCS on a neutron target makes the measurement of this observable very important for the experimental GPD program of Jefferson Lab. Model predictions show that for kinematics that will be available with CLAS12 this asymmetry can be comparable in size to the one obtained for proton DVCS. In order to measure this reaction ensuring its exclusivity, the detection of the recoil neutron, which will be mostly emitted at backwards angles, is necessary. We plan to construct a neutron detector, consisting in a barrel of scintillators coupled at their front ends with u-turn light guides and read out at their back sides by ordinary PMTs connected via 1-m-long bent light guides and placed in the low-field region of the CND. Our GEANT4-based simulations show that the efficiencies obtainable with this detector and its photon-rejection capabilities will be sufficient to collect reasonable statistics for the nDVCS reaction using 80 days of beam time. A three-layer prototype of the CND is under construction. This detector could also be used in other experiments requiring the detection of the recoil neutron, and it can also be useful for the

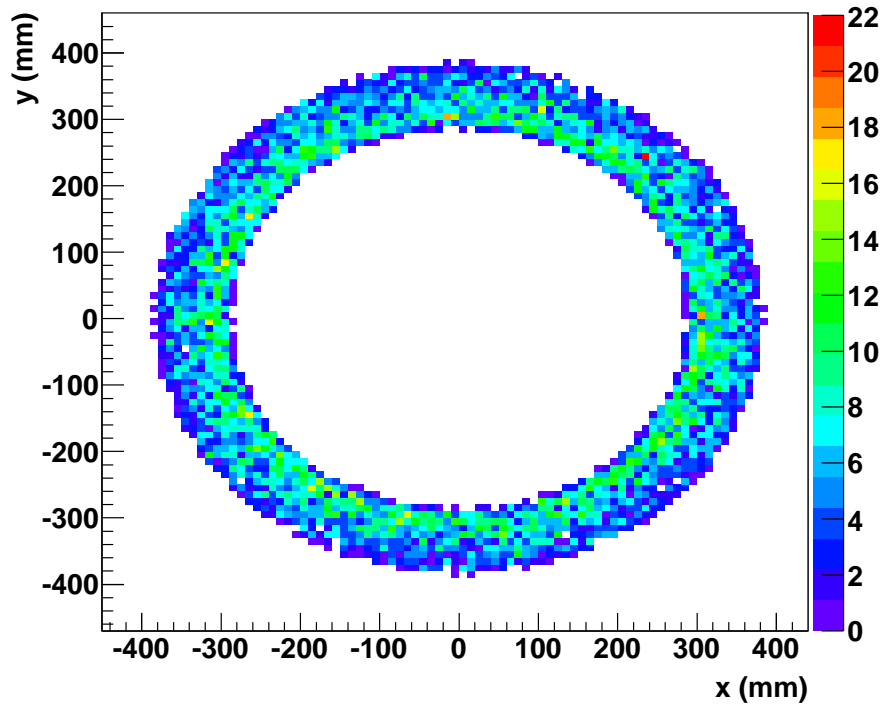


Figure 39: Event distribution for the electromagnetic background in the CND, as a function of the  $x$  and  $y$  coordinates in the lab frame ( $z$  being the beam direction), without any cut on the deposited energy. It can be seen that the majority of the events are concentrated in the innermost layers of the CND.

PID of charged particles via measurement of  $dE/dx$ .

# 11 Appendix: details on simulation and reconstruction

## 11.1 Digitisation of signals from CND paddles (in GEMC)

GEMC currently accumulates all energy-loss steps within a 4 ns time-window into one hit. The digitisation of the signals from the CND paddles follows the following procedure.

For the energy digitisation (ADCs), the calculation of the deposited energy which will be converted into light,  $E_b$ , for EACH STEP  $s$  in the hit is done as follows:

$$E_b = \frac{E_{dep}}{(1 + B * E_{dep}/step_l)} \quad (18)$$

where  $E_{dep}$  is the deposited energy,  $B$  is Birk's constant (which depends on the material), and  $step_l$  is the length of the step — calculated from the difference of the vectors of the current and previous step positions (except for the first step, where the first and second step positions are taken).

The attenuated energies arriving at the PMTs attached to the ends of the scintillator paddles,  $E_l$ ,  $E_r$  (for left and right ends of paddle),  $E_d$  (where  $d$  stands for “direct”),  $E_n$  (“neighbor”, for the u-turn configuration) are summed, for each hit, over the deposit from each step making up the hit:

The calculation for  $E_l$ ,  $E_r$  and  $E_d$  follows the same formula, e.g., for  $E_r$  we have:

$$E_r = \sum_s E_b/2 * e^{(-d_r/l_{att})} * L_{coll} \quad (19)$$

where  $s$  is the index of the particular step,  $d_r$  is the distance from the step position to the end of the scintillator,  $l_{att}$  is the attenuation length in the material ( $l_{att} = 3$  m) and  $L_{coll}$  is the light collection efficiency (fraction of photons which make it into the PMT).  $L_{coll}$  is calculated as the cross-sectional area of the PMT divided by the cross-sectional area of the paddle, and therefore varies for each radial layer.

For the case of  $E_n$ :

$$E_n = \sum_s E_b/2 * e^{(-(d_r+l)/l_{att})} * L_{bend} * L_{coll} \quad (20)$$

where  $l$  is the whole length of the paddle and  $L_{bend}$  is the energy fraction lost at the u-turn bend connecting the neighbouring paddles. Its values, 0.5, is deduced from the measurements on the one-layer prototype carried out in Orsay (see Fig. 24).

The conversion of the energy into ADC values follows the same method for all four ADC readings (ADCL, ADCR, ADCD, ADCN):

$$ADC = P(E * yield * Q_{eff}) * gain * C_{ADC} + ped \quad (21)$$

where  $E$  is one of  $E_r$ ,  $E_l$ ,  $E_d$  or  $E_n$ ,  $yield$  is the light yield (number of photons produced in the scintillator per unit of deposited energy, namely 10000/MeV),  $Q_{eff}$  ( $=0.2$ ) is the quantum efficiency of the PMT (fraction of photoelectrons produced per photon),  $gain$  is the PMT gain ( $=0.08$  pC/photoelectron),  $C_{ADC}$  ( $=10$ /pC) is the conversion factor from charge to ADC



channels,  $ped$  is the ADC pedestal (currently set to 0) and  $P(m)$  is the Poisson distribution function with a mean  $m$ , that smears the number of photoelectrons produced by each hit.

The original treatment of time of the hit in Gemc was to take an average of the signal time from all the steps. Since a TDC will trigger when the analogue signal reaches a particular level, the mean over all times overestimates the actual time. Without knowing the shape of the total signal from all the steps in a hit as it arrives at the TDC we cannot deduce the time precisely, but we have chosen to set it to the time of the first step in the hit passing a given energy deposition threshold, as this may be closer to the true time the TDC will trigger at than the mean.

The time of arrival of the signal at the PMT is calculated in a similar way for  $l$ ,  $r$  and  $d$ , taking the time of the first step in the hit above a 100-keV threshold. For  $r$ , for example:

$$t_r = T + d_r/v_{eff} \quad (22)$$

where  $T$  is the time the first energy deposit (first step) in the hit happened (with respect to the event start time),  $d_r$  is as before the distance from the first step energy deposit to the right end of the paddle and  $v_{eff}$  is the effective velocity of light in the scintillator material.

For  $t_n$ , the calculations is:

$$t_n = T + (d_r + l)/v_{eff} + d_u/v_{eff} \quad (23)$$

where  $d_u$  is the effective distance through the u-turn light guide.

The time is then digitised (in the same way for all four TDC branches, TDCL, TDCR, TDCLD, TDCN). For TDCR for example:

$$TDCR = t_r + G(0, A/\sqrt{E_r}) * C_{TDC} \quad (24)$$

where  $G(\text{mean}, \text{sigma})$  is a Gaussian distribution function,  $A$  is a constant which determines the smearing in the timing. The value chosen for  $A$  ( $A = 0.24 \text{ ns} \cdot \text{MeV}^{-1/2}$ ) is deduced from the time resolution cosmic-rays measurements on the CND one-layer prototype described in Section 5 [29].  $C_{TDC}$  ( $=20/\text{ns}$ ) is the conversion factor from time to TDC channels.

## 11.2 Hit reconstruction

The algorithm for the choice of the “good hit” is here described.

Let us assume paddle 1 is optically coupled to paddle 2. We get  $N1$  signals in TDC of paddle 1 and  $N2$  signals in TDC of paddle 2. The possible combinations one can have are:

- Case A: a signal from a "direct" hit in paddle 1 is reconstructed along with a signal from a "direct" hit in paddle 2. This is wrong.
- Case B: a signal from a "direct" hit in paddle 1 is reconstructed along with a signal from another "direct" hit in the same paddle, propagated to paddle 2. This is also wrong.
- Case C: a signal from a "direct" hit in paddle 1 is reconstructed along with a signal from the same hit propagated to paddle 2. This is right.
- Case D: a signal registered in paddle 1, but it actually propagated from "direct" hit in paddle 2, which was then reconstructed with a signal registered in paddle 2 which had propagated from "direct" hit in paddle 1. This is obviously also wrong.

If only one hit was registered in paddle 1, and no hits in its neighbour paddle, then cases A, B and D are not an issue. However, it is possible that the reconstruction will fail anyway if the signal from the "direct" hit was registered but its propagation to neighbour wasn't (because of energy attenuation perhaps it just didn't make it past the threshold, for example). Those hits are lost.

For each "decent hit" (having energy deposit above zero and the time in its "direct" paddle's TDC reading something physical, not zero or an unstopped TDC value), one needs to determine whether its coupled neighbour is to its left or right. Then an array is filled with all the physical hits in the neighbour and in the same paddle (discarding those that have 0 energy deposit or unphysical TDC times (zero or unstopped TDC)). These hits are called "partners".

Next, for each hit, one iterates through the array of partners. If a partner is a neighbour, one has to take its "direct" TDC time  $tp$  (as recorded in its paddle). If a partner is from the same paddle as the hit in question, one must take its propagated time  $tp$  to neighbour.

We are now working with two time values – the one just selected from the partner,  $tp$ , and the hit's "direct" time,  $th$  (for cases A, and B). For case D, one takes the propagated time from the hit to the neighbour's paddle ( $th$ ), and the partner's propagated time to the hit's paddle ( $tp$ ). One then labels each of the two times as either "time in the paddle where hit happened" or "time propagated to neighbour's paddle", based upon which one is smaller. The  $z$ -position of the hit is reconstructed following this assumption. If  $z$  is out of the dimension of the paddle (-33cm to 33cm), the chosen combination was obviously wrong, so it is discarded and one moves to the next partner. This is what mostly happens for cases A, B and D above. Once one has exhausted all partners, also case C (the real answer) is processed. One reconstructs the hit based on its "direct" time and its propagated time to neighbour. If that gives an unphysical result for  $z$  (or maybe the propagated signal was missing), then that combination is discarded.

After processing all the possible combinations, *goodcomb* is the number of good combinations for that hit, i.e.: possible combinations of signals which yield physical values of  $z$ . If *goodcomb* > 1 we have an ambiguity on how to reconstruct the hit. The hit is discarded. If *goodcomb* = 0, there is no good combination, the hit is also discarded. A hit is kept only if *goodcomb* = 1. One then iterates through such hits, reconstructing  $z$ , TOF and energy deposited for all the unambiguous cases. Next, all these remaining good reconstructed hits are put in order of ascending TOF. The "best hit" is the first "good" hit over an energy threshold, below a time cut. From this hit one gets the TOF,  $z$  and energy deposit of the event.

To obtain the TOF, we calculate  $T_{adjusted}$  as:

$$T_{nadj} = T_n - (p_l + d_u)/v_{eff}; \quad (25)$$

where  $d_u$  is the path length through the u-turn bit (estimate of 8cm),  $v_{eff}$  is effective velocity,  $p_l$  is the length of the paddle, and

$$T_n = \frac{TDCN}{C_{TDC}}. \quad (26)$$

Then we can extract  $z$  as:

$$z_{ave} = (T_d - T_{nadj}) * v_{eff}/2 \quad (27)$$

The value of the TOF is then calculated based on info from both sides:

$$TOF_{true} = T_d - (p_l/2 + z_{ave})/v_{eff} \quad (28)$$

$$TOF_{nadjtrue} = T_{nadj} - (p_t/2 - z_{ave})/v_{eff} \quad (29)$$

Get an average TOF of these:

$$TOF_{true} = (T_{dtrue} + T_{nadjtrue})/2 \quad (30)$$

This quantity is then used to compute  $\beta$ , the momentum and  $\theta$  for the event (see Sections 6.2 and 6.3).

To obtain the energy deposited in the event, one uses the ADC value as follows:

$$E_d = \frac{ADC D}{C_{ADC} \cdot gain \cdot yield \cdot Q_{eff} \cdot L_{coll}} \quad (31)$$

## References

- [1] D. Müller, D. Robaschik, B. Geyer, F.-M. Dittes, and J. Horejsi, Fortschr. Phys. **42** (1994) 101.
- [2] X. Ji, Phys. Rev. Lett. **78** (1997) 610; Phys. Rev. D **55** (1997) 7114.
- [3] A.V. Radyushkin, Phys. Lett. B **380** (1996) 417; Phys. Rev. D **56** (1997) 5524.
- [4] J.C. Collins, L. Frankfurt and M. Strikman, Phys. Rev. D **56** (1997) 2982.
- [5] K. Goeke, M. V. Polyakov and M. Vanderhaeghen, Prog. Part. Nucl. Phys. **47** (2001) 401.
- [6] M. Diehl, Phys. Rept. **388** (2003) 41.
- [7] A.V. Belitsky, A.V. Radyushkin, Phys. Rept. **418** (2005) 1.
- [8] M. Guidal, Eur. Phys. J. A **37** (2008) 319.
- [9] C. Muñoz Camacho et al., Phys. Rev. Lett. **97**, 262002 (2006).
- [10] F.-X. Girod et al., Phys. Rev. Lett. **100**, 162002 (2008).
- [11] A. Airapetian et al, arXiv:0802.2499.
- [12] JLab approved experiment E-05-114: “Deeply Virtual Compton Scattering at 6 GeV with polarized target and polarized beam using the CLAS detector”; spokespersons: A. Biselli, L. Elhouadrhiri, K. Joo and S. Niccolai.
- [13] JLab (conditionally) approved experiment E-08-021: “Deeply Virtual Compton Scattering at 6 GeV with transversely polarized target using the CLAS detector”; spokespersons: H. Avakian, V. Burkert, M. Guidal, R. Kaiser and F. Sabatié.
- [14] JLab approved experiment E-06-003: “Deeply Virtual Compton Scattering with CLAS at 6 GeV”; spokespersons: V. Burkert, L. Elhouadrhiri, M. Garçon, R. Niyazov and S. Stepanyan.
- [15] JLab approved experiment E-07-007: “Complete separation of Deeply Virtual Photon and  $\pi^0$  electroproduction observables of unpolarized protons”; spokespersons: C. Munoz Camacho, J. Roche, C. Hyde-Wright and P.-Y. Bertin.
- [16] JLab approved experiment E-12-06-114: “Measurements of Electron-Helicity Dependent Cross Sections of Deeply Virtual Compton Scattering with CEBAF at 12 GeV”, spokespersons: C. Hyde-Wright, B. Michel, C. Munoz Camacho and J. Roche.
- [17] JLab approved experiment E-12-06-119: “Deeply Virtual Compton Scattering with CLAS at 11 GeV”, spokespersons: V. Burkert, L. Elouadrhiri, M. Garçon, M. Holtrop, D. Ireland, K. Joo, W. Kim, F. Sabatié.
- [18] M. Mazouz et al., Phys. Rev. Lett. **99**, 242501 (2007).
- [19] M. Vanderhaeghen, P.A.M. Guichon, M. Guidal, Phys. Rev. D **60**, 094017 (1999).
- [20] M. Guidal, M. V. Polyakov, A. V. Radyushkin and M. Vanderhaeghen, Phys. Rev. D **72**, 054013 (2005).
- [21] A. El Aloui and E. Voutier, private communication.
- [22] A.V. Belitsky, D. Müller, A. Kirchner, Nucl. Phys. B **629** (2002) 323-392.

- [23] H. Avakyan, private communication.
- [24] M. Lacombe et al., Phys. Rev C **21** (1980) 861.
- [25] R. De Vita, private communication.
- [26] S. Niccolai et al., JLab letter of intent LOI12-09-001.
- [27] NIM A **564** (2006) 204-211.
- [28] R. De Vita, wiki page (link?).
- [29] G. Hull, private communication.
- [30] M. Ungaro, private communication.
- [31] S. Niccolai, [http://clasweb.jlab.org/rungroups/e1-dvcs/wiki/index.php/CLAS12 neutron detector:update on simulation](http://clasweb.jlab.org/rungroups/e1-dvcs/wiki/index.php/CLAS12_neutron_detector:update_on_simulation) (September 2008).
- [32] D. Sokhan, <http://clasweb.jlab.org/wiki/index.php/Daria> .
- [33] M. Mirazita and R. De Vita, private communication.
- [34] S. Koutsnezov, private communication.
- [35] E. Skau and S. Stepanyan, CLAS-NOTE 020-2007.
- [36] B. Genolini (IPN Orsay), private communication.
- [37] T. Nguen Trung (IPN Orsay), private communication.
- [38] [http://clasweb.jlab.org/rungroups/e1-dvcs/wiki/index.php/CLAS12 neutron detector: update 28 October 2009 Lifetime of MCP PMTs](http://clasweb.jlab.org/rungroups/e1-dvcs/wiki/index.php/CLAS12_neutron_detector:_update_28_October_2009_Lifetime_of_MCP_PMTs)
- [39] arXiv:1004.1940 [hep-ph].
- [40] E. Fuchey et al., arXiv:1003.2938 [nucl-exp].
- [41] I. Bedlinski, V. Koubarovski, private communication.
- [42] M. Hoek and B. Seitz (Glasgow), private communication.
- [43] R. De Vita, [http://www.jlab.org/ devita/bgonly.ppt](http://www.jlab.org/devita/bgonly.ppt).